

Flying-Saucer-Shaped Nanoheterojunctions with Enhanced Colorectal Tumor Accumulation for Increased Oxidative Stress and Immunometabolic Regulation

Ya Ma, Yingui Cao, Menghang Zu, Qiang Gao, Ga Liu, Jianying Ji, Haiting Xu, Qiang Yang, Xiaoxiao Shi,* Rui L. Reis, Subhas C. Kundu, Ji Zheng, Zhou Li,* and Bo Xiao*

The treatment outcomes of nanomedicines against colorectal cancer are severely restricted by their insufficient accumulation in the tumor tissues, unsatisfactory antitumor effect, and weak immunometabolic modulation. To address these issues, flying-saucer-shaped nanoheterojunctions by coating copper oxide (Cu_xO) onto the surface of PEGylated zinc oxide (ZnO) nanoparticles are constructed. When exposed to ultrasound, the resultant $\text{Cu}_x\text{O}@Zn\text{O}$ nanoheterojunctions exhibit increased locomotor activities, facilitating colorectal mucus infiltration, deep tumor penetration, and tumor cell internalization. The decoration of Cu_xO suppresses the rapid recombination of electrons and holes in $\text{Cu}_x\text{O}@Zn\text{O}$ exposed to ultrasound, promoting the production of singlet oxygen and hydroxyl radical, which are generated by Cu_xO through a Fenton-like chemodynamic reaction and $\text{Cu}_x\text{O}@Zn\text{O}$ through sonodynamic reaction. After rectal administration, the sono-chemodynamic $\text{Cu}_x\text{O}@Zn\text{O}$ plus PD-L1 antibodies effectively inhibit the growth of orthotopic and distant tumors. It elicits immunometabolic responses by inducing immunogenic cell death, activating the interferon genes signaling pathway stimulator, and inhibiting glucose transport and the glycolytic signaling pathways. This combined modality also increases the proportion of beneficial microbes (e.g., *Bifidobacterium*) and decreases the abundance of harmful microorganisms (e.g., *Romboutsia*) in the intestine. This treatment modality ($\text{Cu}_x\text{O}@Zn\text{O}$ plus ultrasound and PD-L1 antibodies) is a promising strategy for the synergistic treatment of colorectal cancer.

1. Introduction

Sonodynamic therapy (SDT), triggered by low-intensity ultrasound (US), has emerged as a promising noninvasive, tissue-penetrating approach for the treatment of various deep-seated cancers, such as prostate cancer, endometrial cancer, and breast cancer.^[1,2] This sonosensitizer-based therapeutic approach can catalyze surrounding oxygen (O_2) and H_2O to produce cytotoxic reactive oxygen species (ROS) that effectively kill tumor cells.^[3,4] Unfortunately, traditional organic small-molecule sonosensitizers (e.g., porphyrin derivatives, chlorine 6, and indocyanine green) and organic micro/nanoparticle sonosensitizers suffer from low bioavailability, short half-life, insufficient tumor accumulation, and poor chemical/physiological stability, which impede the therapeutic efficacy of SDT.^[5,6] In comparison with the short blood half-life and non-negligible phototoxicity and photostability of traditional organic small-molecule sonosensitizers and organic micro/nanoparticle sonosensitizers with poor chemical/physiological stability, metal-based inorganic piezoelectric

Y. Ma, J. Zheng
Department of Urology
Urologic Surgery Center
Xinqiao Hospital
Third Military Medical University (Army Medical University)
Chongqing 400037, China
Y. Ma, Y. Cao, M. Zu, Q. Gao, G. Liu, H. Xu, Q. Yang, X. Shi
College of Sericulture
Textile and Biomass Sciences
Southwest University
Chongqing 400715, China
E-mail: xxshi7@swu.edu.cn

J. Ji, Z. Li
Beijing Institute of Nanoenergy and Nanosystems
Chinese Academy of Sciences
Beijing 101400, China
E-mail: zli@binn.cas.cn
R. L. Reis, S. C. Kundu
3Bs Research Group
I3Bs — Research Institute on Biomaterials
Biodegradables and Biomimetics
University of Minho
Headquarters of the European Institute of Excellence on Tissue Engineering and Regenerative Medicine
AvePark
Barco, Guimarães 4805-017, Portugal
R. L. Reis, S. C. Kundu
ICVS/3B's-PT Government Associate Laboratory
Guimarães, Braga 4800-058, Portugal

The ORCID identification number(s) for the author(s) of this article can be found under <https://doi.org/10.1002/adfm.202402164>

DOI: 10.1002/adfm.202402164

semiconductors have been reported to overcome these deficiencies.^[7] However, the yield of US-triggered ROS generation based on inorganic piezoelectric sonosensitizers remains relatively low due to the rapid recombination of electrons (e^-) and holes (h^+).^[8,9] Therefore, developing novel and effective sonosensitizers for enhancing SDT is still urgently desired.

Recently, piezoelectric catalysis has garnered significant attention due to its capacity for inducing polarization in piezoelectric materials and establishing a built-in electric field under mechanical forces.^[10,11] The piezo-potential, acting as a potent electromotive force, facilitates the separation of e^- and h^+ in opposite directions and initiates redox reactions on both conduction band (CB) and valence band (VB), thereby improving the SDT effect.^[12,13] Zinc oxide (ZnO) nanoparticles (NPs), an FDA-approved biomaterial, have been developed for piezocatalysis owing to their high piezoelectric coefficient, excellent biocompatibility, efficient charge transfer, and large specific surface area.^[14,15] However, the intensity of piezoelectric polarization induced by low-frequency US pulses is insufficient to initiate redox reactions. Numerous investigations have been undertaken to augment the piezoelectric characteristics of ZnO nanomaterials, including metal-ion doping, defect introduction, and heterostructure integration, including Au@P-ZnO nanorods,^[16] Pt-ZnO nanorods,^[17] and ZnO-CdS nanocomposites.^[18] Nevertheless, challenges in optimizing their structure and composition remain to be overcome. Systematically analyzing the impacts of structure and composition on piezocatalytic efficiency is instrumental in developing novel approaches for piezoelectric-based catalysis.

Herein, flying-saucer-shaped $Cu_xO@ZnO$ heterostructures were fabricated as piezocatalysts by coating copper oxide (Cu_xO) onto the surface of PEGylated ZnO NPs for enhanced SDT of colorectal cancer (CRC). We investigated their piezoelectric effect and piezocatalytic mechanism under exposure to low-intensity US. As shown in **Scheme 1**, when exposed to low-power US (1 W cm^{-2}), the polarized internal electric field in the $Cu_xO@ZnO$ heterostructures facilitated the separation and migration of e^- and h^+ , resulting in a remarkable band bending. Interestingly, changes in band bending are advantageous for initiating redox reactions and catalyzing the production of singlet oxygen (1O_2) and hydroxyl radical ($\bullet OH$). The Cu_xO not only participates in the formation of heterostructures that enhance piezocatalysis, but also exhibits a weak Fenton-like reaction that catalyzes the production of $\bullet OH$ from over-produced intracellular H_2O_2 . The results from in vitro and in vivo experiments demonstrate that the sono-chemodynamic $Cu_xO@ZnO$ heterostructures effectively suppress colorectal tumor growth and elicit immune responses by inducing apoptosis and immunogenic cell death (ICD) of tumor cells, activating the stimulator of interferon genes (STING) signaling pathway, and inhibiting glucose transport and the glycolytic signaling pathways.

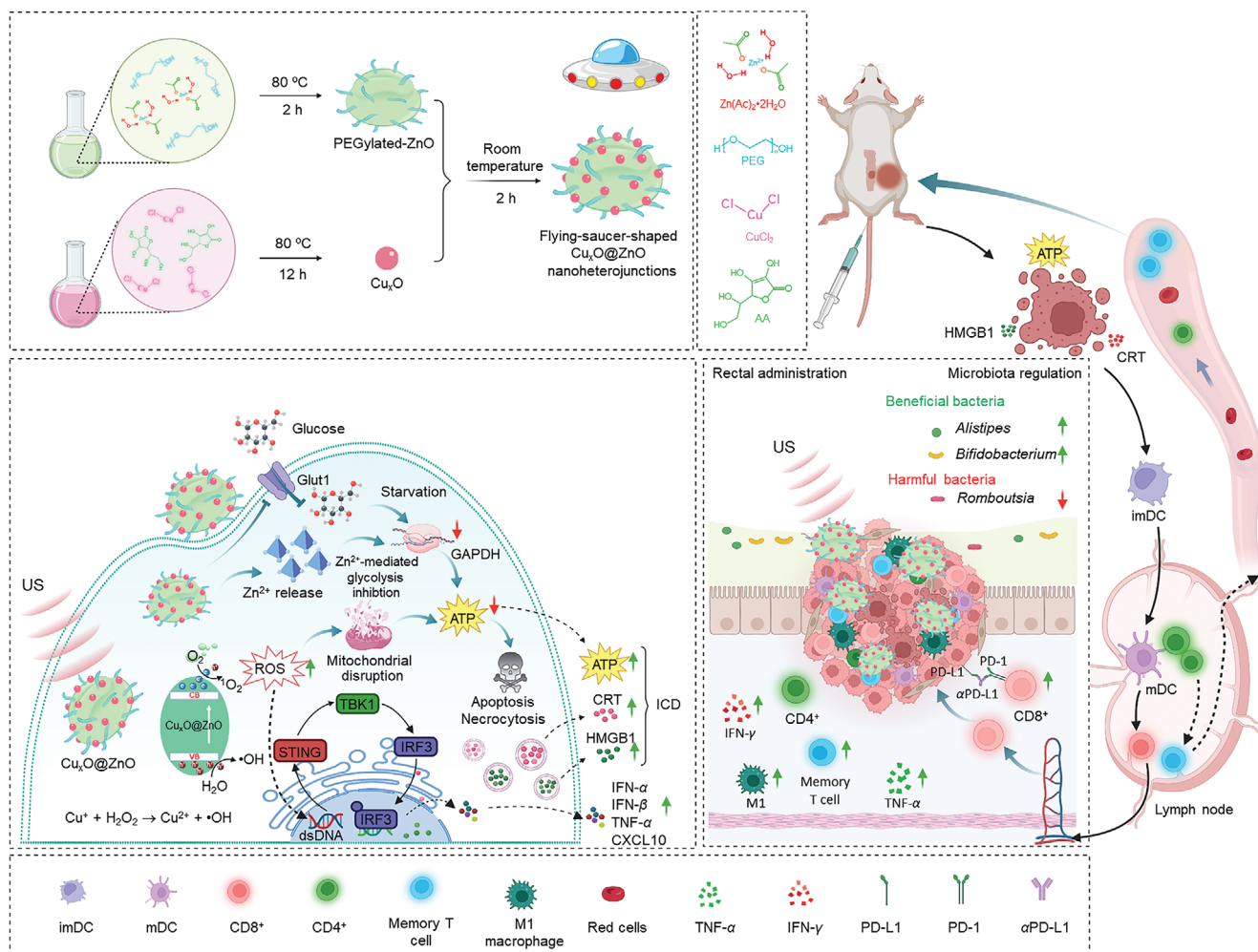
B. Xiao
Department of Pharmacy
Personalized Drug Therapy Key Laboratory of Sichuan Province
Sichuan Provincial People's Hospital
School of Medicine
University of Electronic Science and Technology of China
Chengdu 610054, China
E-mail: bxiao@uestc.edu.cn

2. Results and Discussion

2.1. Fabrication and Physicochemical Characterization of $Cu_xO@ZnO$

ZnO NPs preferentially formed large aggregations, and the introduction of PEG to ZnO NPs facilitated their uniform dispersion in an aqueous solution.^[19,20] Thus, PEGylated ZnO NPs were synthesized and used in the construction of piezoelectric $Cu_xO@ZnO$ nanoheterojunctions. Briefly, PEGylated ZnO and Cu_xO were separately synthesized via a hydrothermal method, followed by compounding Cu_xO onto the surface of PEGylated ZnO to obtain $Cu_xO@ZnO$ NPs. Images from scanning electron microscopy (SEM) and transmission electron microscopy (TEM) showed that the as-prepared PEGylated ZnO NPs had a uniform size distribution, with an average particle size of 294.7 nm (Figure **S1A,B**, Supporting Information). The high-resolution TEM (HRTEM) images further revealed that the crystalline structure of PEGylated ZnO NPs had a lattice-fringe spacing of 0.29 nm that corresponded to their (100) plane (Figure **S1C**, Supporting Information). During the formation of $Cu_xO@ZnO$ heterojunctions, Cu_xO NPs acted as co-catalysts for in situ adsorption on the surface of PEGylated ZnO NPs. The resultant flying-saucer-shaped $Cu_xO@ZnO$ nanoheterojunctions, as depicted in **Figures 1A,B** and **S1D** (Supporting Information), possessed a diameter of 311.7 nm and maintained excellent monodispersity. The size distribution and zeta potential results determined by dynamic light scattering (DLS) initially proved the successful adsorption of Cu_xO onto the PEGylated ZnO surface, as evidenced by a slight increase in particle size (from 349 to 377 nm) and zeta potential (from -21.6 to -19.0 mV), along with a low polydispersity index of <0.300 (Figure **S1E-G**, Supporting Information). The obtained $Cu_xO@ZnO$ nanoheterojunctions could maintain stable in the simulated colonic fluid over 24 h (Figure **S1H**, Supporting Information). Moreover, with Fourier transform infrared spectroscopy (FTIR), we observed a noticeable reduction in the strong, sharp characteristic absorption peak of PEGylated ZnO NPs at 457 cm^{-1} , corresponding to the Zn-O stretching mode in the FTIR spectrum of $Cu_xO@ZnO$ (Figure **S1I**, Supporting Information). This increase can be attributed to the formation of $Cu_xO@ZnO$ nanoheterojunctions.

Furthermore, the energy-dispersive X-ray (EDX) mapping results of $Cu_xO@ZnO$ unequivocally validated the simultaneous presence and uniform distribution of Cu, Zn, and O elements (Figure **1C**). X-ray powder diffraction (XRD) analysis revealed that PEGylated ZnO NPs possessed an amorphous crystal structure (Figure **S1J**, Supporting Information). After adsorbing Cu_xO , the crystal structure of $Cu_xO@ZnO$ nanoheterojunctions, demonstrated a congruent pattern with PEGylated ZnO, ascribed to the presence of the minor deposited Cu_xO . The successful synthesis of PEGylated ZnO and $Cu_xO@ZnO$ heterojunctions was further validated by X-ray photoelectron spectroscopy (XPS). The elemental composition and valence state of the PEGylated ZnO-based NPs is shown in Figure **1D**, revealing the presence of a characteristic peak at 935.3 eV corresponding to Cu 2p in $Cu_xO@ZnO$. By analyzing the high-resolution Cu 2p spectrum of $Cu_xO@ZnO$, the peaks observed at 952.3 and 932.1 eV were attributed to Cu 2p_{1/2} and Cu 2p_{3/2} of Cu^+ , respectively,



Scheme 1. Schematic illustration for the preparation and antitumor mechanism of flying-saucer-shaped $\text{Cu}_x\text{O}@Z\text{nO}$ nanoheterojunctions and the synergistic therapeutic outcomes of $\text{Cu}_x\text{O}@Z\text{nO}$ against CRC. After rectal administration, $\text{Cu}_x\text{O}@Z\text{nO}$ nanoheterojunctions penetrated through the colonic mucus barrier, accumulated in the colorectal tumor tissues, triggered immunogenic death of tumor cells through the generated ROS from sono-chemodynamic $\text{Cu}_x\text{O}@Z\text{nO}$ and Zn^{2+} -mediated glycolytic signaling pathway inhibition, activation of systematic immune responses to suppress orthotopic and distant tumors, increased abundance of beneficial microbes (e.g., *Alistipes* and *Bifidobacterium*), and decreased proportion of harmful microorganisms (e.g., *Romboutsia*) in the intestine. This figure was created with BioRender.com.

while the peaks at 933.6 and 953.8 eV revealed the presence of Cu^{2+} (Figure 1E). This definitive data confirmed the co-existence of Cu_2O and CuO on the surface of PEGylated ZnO. Simultaneously, the valence states of Zn 2p and O 1s of $\text{Cu}_x\text{O}@Z\text{nO}$ showed no noticeable change compared with PEGylated ZnO NPs from high-resolution spectra (Figure 1F,G).

2.2. Cu_xO Adsorption Improves the ROS Generation Efficiency of PEGylated ZnO

ROS, including predominantly $\bullet\text{OH}$ and $^1\text{O}_2$, which exert strong toxic effect against tumor cells, can be produced by sonosensitizers exposed to US pulses.^[21] Cu^+ -mediated Fenton-like chemodynamic reaction also acts as a favorable pathway for catalyzing the generation of $\bullet\text{OH}$ from H_2O_2 . Here, methylene blue (MB) and 1,3-diphenylisobenzofuran (DPBF) were

employed as indicators to assess the generating capability of $\bullet\text{OH}$ and $^1\text{O}_2$ by $\text{Cu}_x\text{O}@Z\text{nO}$ nanoheterojunctions, respectively (Figure 2A). Considering the presence of Cu^+ in $\text{Cu}_x\text{O}@Z\text{nO}$, we initially investigated the chemodynamic performance of PEGylated ZnO and $\text{Cu}_x\text{O}@Z\text{nO}$. As displayed in Figure 2B, the treatment of H_2O_2 and PEGylated ZnO had minimal impacts on the absorbance of MB compared with the PBS control group. However, the co-incubation of $\text{Cu}_x\text{O}@Z\text{nO}$ and H_2O_2 resulted in a noticeable decrease in MB absorbance, indicating that $\text{Cu}_x\text{O}@Z\text{nO}$ possessed chemodynamic catalytic power to produce $\bullet\text{OH}$ because of the presence of Cu_xO . Considering the acidic environment and endogenous H_2O_2 in the tumor microenvironment, we investigated the $\bullet\text{OH}$ production capacity of $\text{Cu}_x\text{O}@Z\text{nO}$ under varying pH and ROS conditions. It was found that the MB absorption intensities markedly diminished in the acidic buffer (pH 6.8 and pH 5.5) and H_2O_2 -contained buffers (1, 5, and 10 mM), suggesting that the

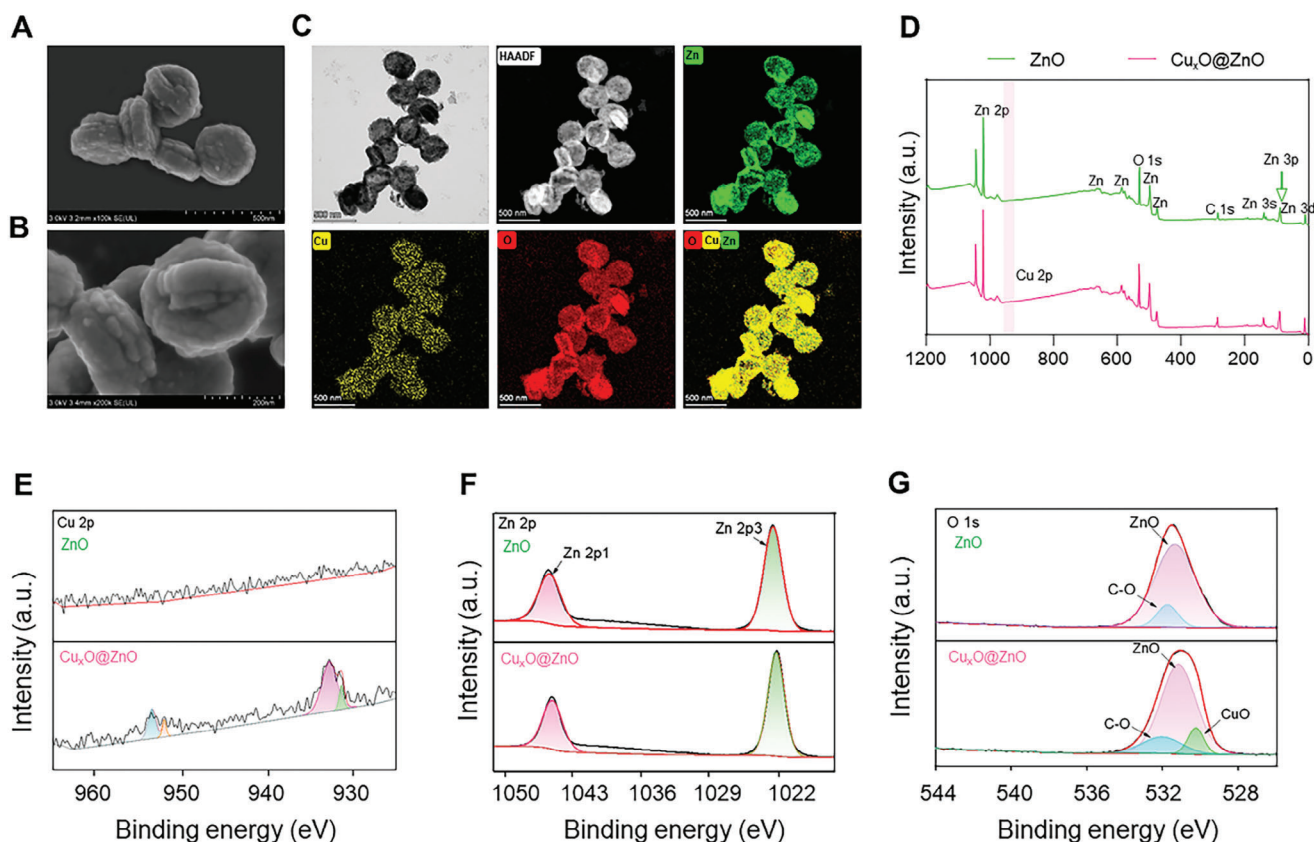


Figure 1. Fabrication and physicochemical characterization of $\text{Cu}_x\text{O}@Zn\text{O}$ nanoheterojunctions. A,B) Representative SEM images of $\text{Cu}_x\text{O}@Zn\text{O}$. C) The representative HRTEM image and EDX element mapping of $\text{Cu}_x\text{O}@Zn\text{O}$. D) XPS spectra of PEGylated ZnO and $\text{Cu}_x\text{O}@Zn\text{O}$. High-resolution E) Cu 2p, F) Zn 2p, and G) O 1s XPS spectra of PEGylated ZnO and $\text{Cu}_x\text{O}@Zn\text{O}$.

Fenton-like catalytic performance of $\text{Cu}_x\text{O}@Zn\text{O}$ was contingent upon the acidity and ROS concentrations (Figure S2A,B, Supporting Information). Therefore, it is envisaged that $\text{Cu}_x\text{O}@Zn\text{O}$ can efficiently produce $\bullet\text{OH}$ in the acidic tumor microenvironment with endogenous H_2O_2 .

Moreover, we benchmarked the $\bullet\text{OH}$ generating performance of $\text{Cu}_x\text{O}@Zn\text{O}$ nanoheterojunctions activated by US. As reported, ZnO NPs, a commonly used piezoelectric material, can generate cytotoxic $\bullet\text{OH}$ and $^1\text{O}_2$ from H_2O and O_2 when exposed to US.^[22,23] This property was verified by an apparent decrease in MB concentrations (Figure S2C, Supporting Information) and a slight increase in the apparent reaction rate constant (k) (Figure S2D, Supporting Information) in the pseudo-first-order degradation kinetics of MB. Interestingly, introducing Cu_xO onto the PEGylated ZnO surface led to a significant increase in $\bullet\text{OH}$ with exposure to US. Statistically, in comparison with PEGylated ZnO, $\text{Cu}_x\text{O}@Zn\text{O}$ nanoheterojunctions achieved a 2.2-fold increase in the generated amount of $\bullet\text{OH}$ and an increased k value (0.0011 min^{-1}), which was 1.4 times larger than that of PEGylated ZnO. These observations suggest that the combination with Cu_xO significantly improves the catalytic performance of PEGylated ZnO.

In addition to $\bullet\text{OH}$ generation, we assessed the $^1\text{O}_2$ production capacity of $\text{Cu}_x\text{O}@Zn\text{O}$ nanoheterojunctions using a DPBF probe. The $^1\text{O}_2$ production efficiency of $\text{Cu}_x\text{O}@Zn\text{O}$ was highest

with US exposure, exhibiting 5.0-fold and 1.4-fold increases compared to the control and the PEGylated ZnO (+ US) groups, respectively (Figure 2C). These results substantiate the notion that the presence of Cu_xO on the surface of $\text{Cu}_x\text{O}@Zn\text{O}$ augments the sonodynamic ability of PEGylated ZnO. The degradation kinetics of DPBF over time revealed a pseudo-first-order reaction profile, and the calculated k value of $\text{Cu}_x\text{O}@Zn\text{O}$ was 0.0055 min^{-1} , which was 2.0-fold more extensive than that of PEGylated ZnO (Figure 2D). They were quantified using MB as a probe to validate the synergistic catalytic effects of the sonodynamic and chemodynamic processes. It was found that $\text{Cu}_x\text{O}@Zn\text{O}$ NPs had a strong capacity to degrade MB molecules, with a degradation rate exceeding 23.7% after undergoing treatment with US and H_2O_2 for 10 min (Figure 2E; Figure S2E, Supporting Information). In contrast, the control and PEGylated ZnO groups exposed to US and H_2O_2 exhibited MB degradation rates of only 1.0% and 10.4%, respectively, which could be attributed to the inadequate generation of $\bullet\text{OH}$. Additionally, the k values of the control and PEGylated ZnO groups exposed to US and H_2O_2 were found to be 4.5- and 2.7-fold lower, respectively, than that of the $\text{Cu}_x\text{O}@Zn\text{O}$ group in the presence of US and H_2O_2 (Figure S2F, Supporting Information). These findings verify that $\text{Cu}_x\text{O}@Zn\text{O}$ nanoheterojunctions possess combined sono-chemodynamic effects, which can produce large amounts of $\bullet\text{OH}$ for killing tumor cells.

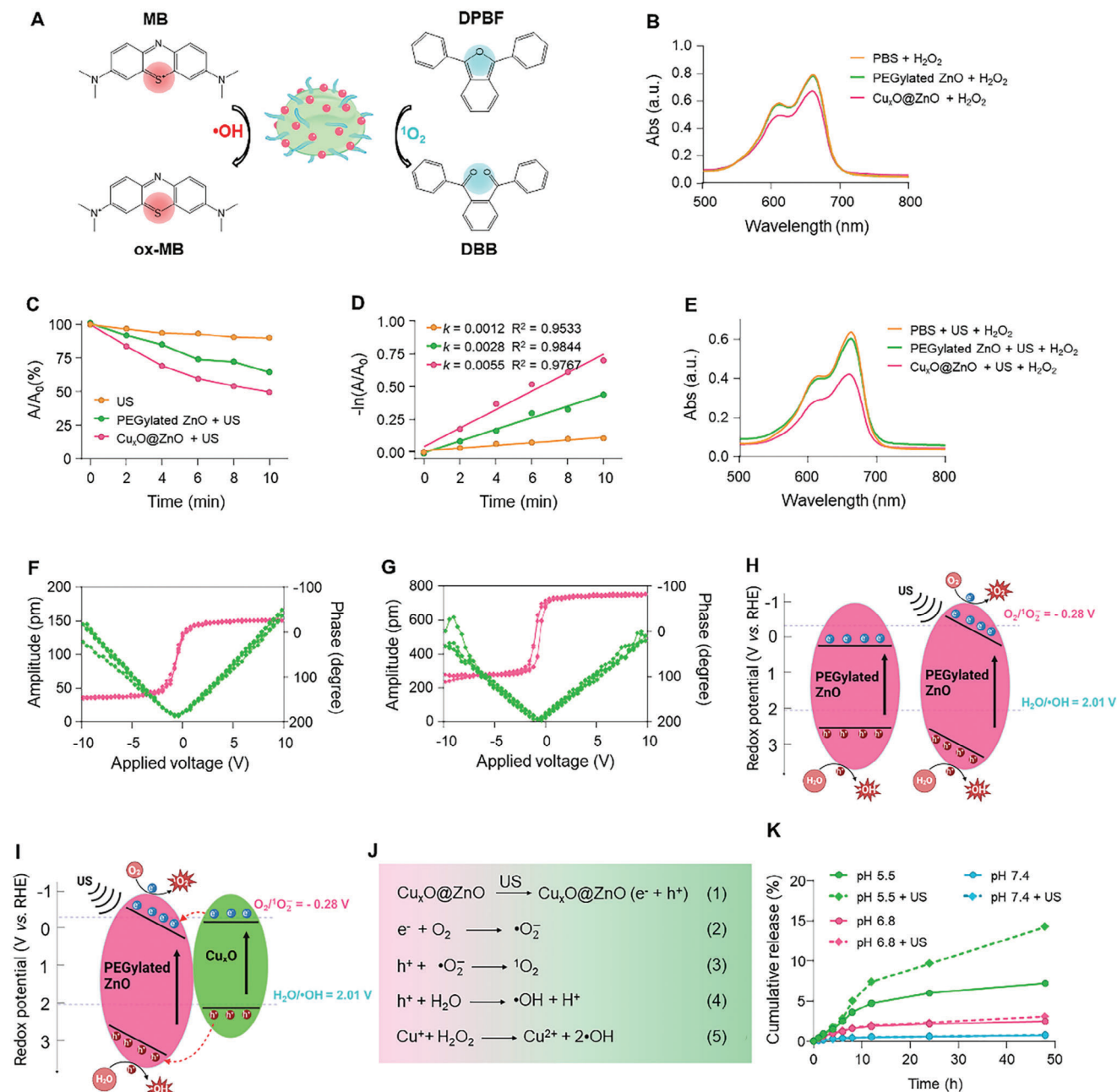


Figure 2. ROS generation processes of Cu_xO@ZnO nanoheterojunctions and the corresponding mechanisms. A) Schematic diagram of ROS generation and detection by the corresponding probes. B) Generation of $\bullet\text{OH}$ in the chemodynamic process measured using MB as the probe. C) Degradation curves and D) kinetic curves of DPBF for detecting $^1\text{O}_2$ during the sonodynamic process. E) Production of $\bullet\text{OH}$ in the sonodynamic and chemodynamic processes using MB as a probe. Amplitude butterfly loop and phase hysteresis loop of F) PEGylated ZnO and G) Cu_xO@ZnO. H) Schematic diagram of the separation and migration of electron–hole pairs in PEGylated ZnO without (left) and with (right) piezotronic effect. I) Schematic diagram of the separation and migration of electron–hole pairs in Cu_xO@ZnO with piezotronic effect. J) Mechanism of Cu_xO@ZnO through US-triggered chemodynamic reaction and Fenton-like reaction. K) The cumulative release profiles of Zn²⁺ from Cu_xO@ZnO, without or with US exposure incubated in the buffers with different pH values (5.5, 6.8, and 7.4) for 48 h.

Although we confirmed the remarkable sonodynamic performance of Cu_xO@ZnO, it is imperative to elucidate its underlying mechanism. For that purpose, we employed piezoelectric force microscopy (PFM) to assess the piezoelectric performance of Cu_xO@ZnO nanoheterojunctions. As shown in Figure 2F,G, the

PFM phase hysteresis loop of Cu_xO@ZnO exhibited a noticeable angle change of 194° at a direct current voltage ranging from 10 to 10 V, surpassing the 175° observed for PEGylated ZnO alone. This result highlights the enhanced piezoelectric activity of Cu_xO@ZnO nanoheterojunctions compared with PEGylated

ZnO NPs. Subsequently, the piezoelectric coefficients (d_{33}) of PEGylated ZnO and $\text{Cu}_x\text{O}@Z\text{nO}$ were determined using a conventional amplitude ‘butterfly loop’ method. Their d_{33} values were computed to be 15.34 and 47.70 pm V⁻¹, respectively, providing further evidence for the superior piezoelectric capacity of $\text{Cu}_x\text{O}@Z\text{nO}$ (Figure S3A,B, Supporting Information).

We also measured the band structures of Cu_xO , PEGylated ZnO, and $\text{Cu}_x\text{O}@Z\text{nO}$ by UV–vis diffuse reflectance spectroscopy. Based on the Kubelka–Munk function, the bandgap energies (E_g) of PEGylated ZnO, Cu_xO , and $\text{Cu}_x\text{O}@Z\text{nO}$ were determined to be 2.69, 2.72, and 3.25 eV, respectively. Their valence band (VB) energies were measured as 2.54, 2.45, and 3.49 eV by analyzing the XPS valence band spectra (Figures S4 and S5, Supporting Information). The conduction band (CB) values of PEGylated ZnO and Cu_xO were calculated to be 0.15 and 0.27 eV, respectively, from the difference between VB and E_g . Since the VB position (2.54 V) of PEGylated ZnO was higher than the $\text{H}_2\text{O}/\bullet\text{OH}$ redox potential (2.01 V vs RHE), the holes (h^+) generated in the VB of PEGylated ZnO upon US treatment were expected to react with water, resulting in $\bullet\text{OH}$ generation (Figure 2H). However, the CB energy level of PEGylated ZnO (0.15 eV) was much more positive than the reduction potential of $\text{O}_2/\bullet\text{O}_2$ (0.28 V vs RHE), impeding the $\bullet\text{O}_2$ generation from O_2 . We further found that the maximum piezoelectric potential generated by PEGylated ZnO under US treatment was measured to be 0.67 V (Figure S6, Supporting Information), which could facilitate band bending, leading to a negative CB edge and promoting the catalytic generation of $^1\text{O}_2$ from O_2 (Figure 2H). Unfortunately, the rapid recombination of electron-hole pairs in the single-PEGylated ZnO limited the ROS generation efficiency.

Both PEGylated ZnO and Cu_xO in the $\text{Cu}_x\text{O}@Z\text{nO}$ heterojunctions could be excited by US, effectively inducing the separation of electron-hole pairs. This occurs because the low energy of PEGylated ZnO leads to electron migration from the CB of Cu_xO to the CB of PEGylated ZnO and hole migration from the VB of PEGylated ZnO to the VB of Cu_xO , effectively suppressing the recombination of electron-hole pairs (Figure S7, Supporting Information). Moreover, US exposure induced a maximum piezoelectric potential of 0.67 V between the opposite sides of the $\text{Cu}_x\text{O}@Z\text{nO}$ heterojunctions, as demonstrated by a typical finite element modeling (FEM) simulation (Figure S6, Supporting Information). This US-triggered potential difference resulted in band bending, which facilitated the migration of electrons and holes from the CB and VB of Cu_xO to those of PEGylated ZnO, thereby enhancing the catalytic generation of $\bullet\text{OH}$ and $^1\text{O}_2$ (Figure 2I). The piezoelectric effect of $\text{Cu}_x\text{O}@Z\text{nO}$ heterojunctions enhanced the separation and migration of charges and orchestrated a reconfiguration of their energy bands. Mechanistically, the continuously updated built-in electric field during US exposure significantly enhanced reduction potentials, amplifying ΔE between the energy band level and the redox potential. This implies an augmented capacity of $\text{Cu}_x\text{O}@Z\text{nO}$ for ROS generation. Figure 2J illustrates how the US induced the polarization of PEGylated ZnO and $\text{Cu}_x\text{O}@Z\text{nO}$, effectively separating electrons and holes (Equation 1). The e^- and h^+ reacted with surrounding O_2 and H_2O_2 to generate $^1\text{O}_2$ and $\bullet\text{OH}$ (Equations 2–4). Meanwhile, $\text{Cu}_x\text{O}@Z\text{nO}$ triggered a subtle Fenton-like reaction for the catalytic production of $\bullet\text{OH}$ from H_2O_2 (Equation 5). The promising sonodynamic and chemodynamic

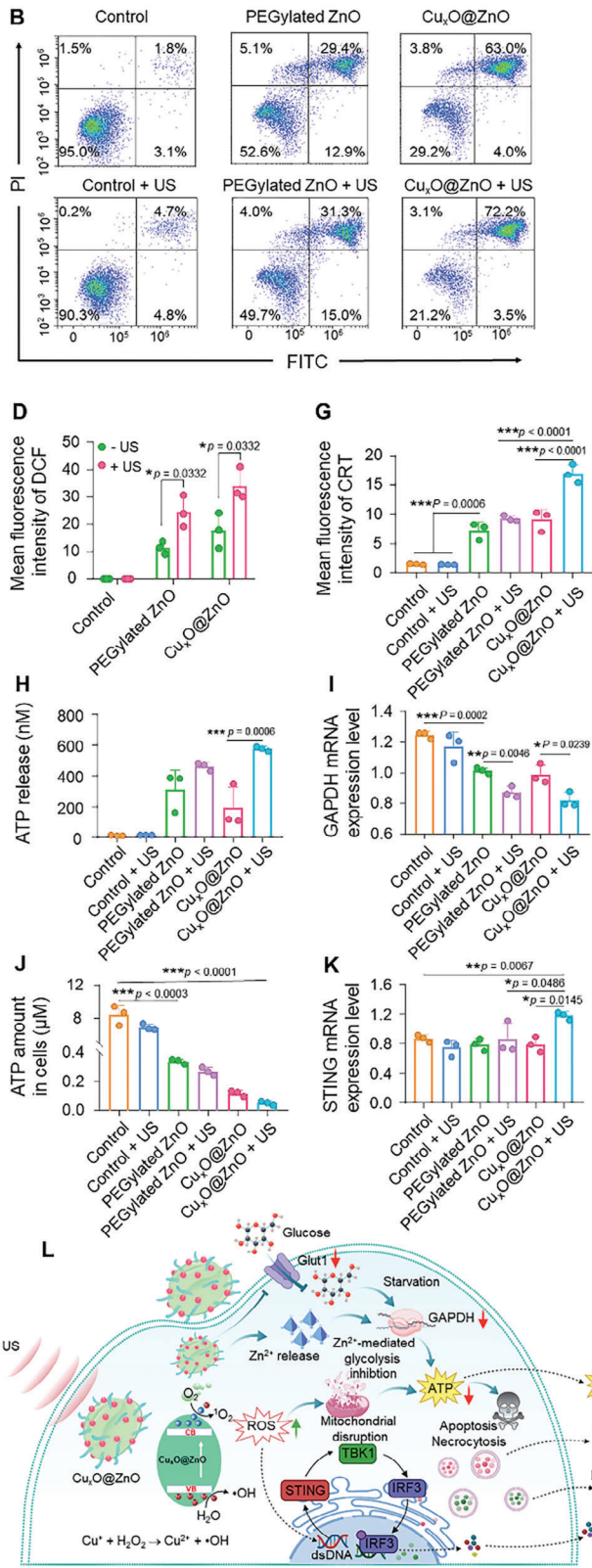
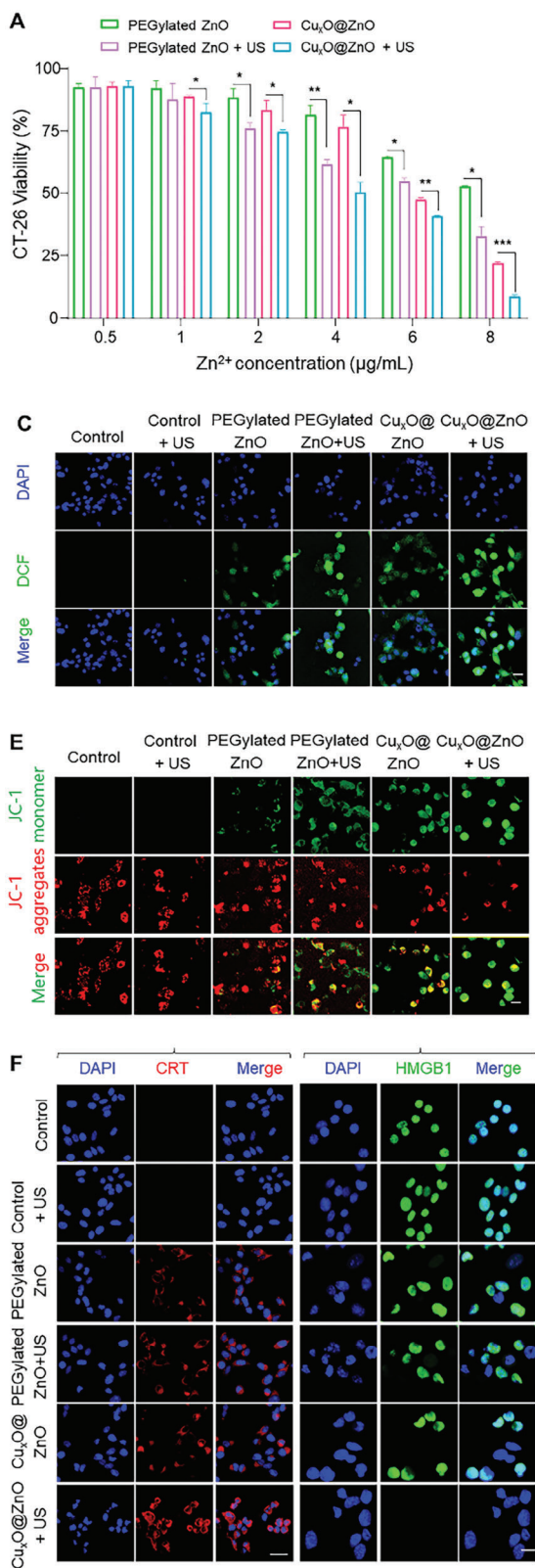
effects of $\text{Cu}_x\text{O}@Z\text{nO}$ make evaluating its antitumor efficacy worthwhile.

Subsequently, we evaluated the release profile of Zn^{2+} from $\text{Cu}_x\text{O}@Z\text{nO}$. Figure 2K shows that the Zn^{2+} release rate was accelerated in the acidic tumor environment with exposure to US, owing to the acid sensitivity of metal oxides and the US-enhanced surface vibration of $\text{Cu}_x\text{O}@Z\text{nO}$ NPs. Compared with the negligible Zn^{2+} release in the typical physiological environment of pH 7.4 (0.8%) and the slightly acidic colonic environment of pH 6.8 (2.5%), a cumulative Zn^{2+} release of 7.2% was determined in the acidic environment of colorectal tumors (pH 5.5). The US treatment further augmented the amount of cumulative Zn^{2+} released to 14.3% following 48 h incubation in an acidic environment (pH 5.5). These results demonstrate that acidic conditions and US treatment facilitate the release of Zn^{2+} , which is necessary for inhibiting glycolysis and inducing tumor cell apoptosis.

2.3. $\text{Cu}_x\text{O}@Z\text{nO}$ Exerts Synergistic Anti-CRC Effects In Vitro

The intracellular endocytosis of nanotherapeutics is a prerequisite for their antitumor effects.^[24] Thus, we determined the cellular uptake profiles of $\text{Cu}_x\text{O}@Z\text{nO}$ nanoheterojunctions qualitatively and quantitatively using confocal laser scanning microscopy (CLSM) and flow cytometry (FCM), respectively. The cellular internalization was visually tracked through the green fluorescence emitted by FITC-labeled $\text{Cu}_x\text{O}@Z\text{nO}$. It was observed that the endocytosis of FITC-labeled $\text{Cu}_x\text{O}@Z\text{nO}$ by CT-26 cells followed a time-dependent pattern, and the green fluorescence intensities of cells increased with longer co-incubation times (1, 2, and 4 h) (Figure S8A, Supporting Information). Notably, upon US treatment, more pronounced green fluorescence signals were observed in CT-26 cells, suggesting that US treatment could promote phagocytosis of FITC-labeled $\text{Cu}_x\text{O}@Z\text{nO}$ (Figure S8B, Supporting Information). We also found that the phagocytic efficiency of FITC-labeled $\text{Cu}_x\text{O}@Z\text{nO}$ determined by FCM was consistent with the CLSM results. In particular, after a 4 h co-incubation and US exposure, the uptake percentage of FITC-labeled $\text{Cu}_x\text{O}@Z\text{nO}$ by CT-26 cells reached 86.5%, while the mean fluorescence intensity (MFI) was 24,423.1. Both values were significantly higher than those of the FITC-labeled $\text{Cu}_x\text{O}@Z\text{nO}$ -treated cells without US (Figure S8C,D, Supporting Information). In addition, we quantified the intracellular concentration of Zn^{2+} following a 4 h co-incubation of $\text{Cu}_x\text{O}@Z\text{nO}$ with CT-26 cells using atomic absorption spectroscopy. Figure S9 (Supporting Information) revealed that US resulted in a significant 2.0-fold increase in the intracellular Zn^{2+} concentration in $\text{Cu}_x\text{O}@Z\text{nO}$ -treated cells, compared with no-US control. These results demonstrate that US treatment can efficiently increase the cellular uptake efficiency of $\text{Cu}_x\text{O}@Z\text{nO}$ and the intracellular Zn^{2+} concentration.

Next, the antitumor activities of various therapeutic modalities were evaluated at equal Zn^{2+} concentrations by the 3-(4, 5-dimethylthiazol-2-yl)-2, 5-diphenyl tetrazolium bromide (MTT) assay. As illustrated in Figure 3A, the therapeutic superiority of $\text{Cu}_x\text{O}@Z\text{nO}$ over PEGylated ZnO gradually became evident with increasing Zn^{2+} doses, particularly when assisted by US. At a Zn^{2+} concentration of 8 $\mu\text{g mL}^{-1}$, $\text{Cu}_x\text{O}@Z\text{nO}$ exhibited apparent cytotoxicity against CT-26 cells, reducing cell viability to



22.1%. It is credible that combining $\text{Cu}_x\text{O}@Z\text{nO}$ with US exposure exerted the most substantial cytotoxic effect against CT-26 cells. Moreover, we conducted a comprehensive antitumor analysis of PEGylated ZnO and $\text{Cu}_x\text{O}@Z\text{nO}$ using live/dead cell double staining and a flow cytometric apoptosis assay. The simultaneous presence of a screen full of red (dead) cells and sporadic green (live) cells was observed in the $\text{Cu}_x\text{O}@Z\text{nO}$ (+ US) group (Figure S10, Supporting Information). The presence of late apoptotic cells (72.2%) in the $\text{Cu}_x\text{O}@Z\text{nO}$ (+ US) group warranted particular attention, as it exhibited 37.8-, 2.5-, and 1.2-fold higher levels than those in the control, PEGylated ZnO (+ US), and $\text{Cu}_x\text{O}@Z\text{nO}$ (+ US) groups, respectively (Figure 3B). In addition, we tested the cytotoxicity of various NPs against the non-tumor L929 cell line. We found that the viability of L929 cells remained above 70.0% when incubated with PEGylated ZnO and $\text{Cu}_x\text{O}@Z\text{nO}$ at a Zn^{2+} concentration of $8 \mu\text{g mL}^{-1}$, irrespective of exposure to US (Figure S11, Supporting Information), illustrating that both PEGylated ZnO and $\text{Cu}_x\text{O}@Z\text{nO}$ with or without US treatment exhibited minimal toxicity against the normal cells. Collectively, these findings validate the hypothesis that $\text{Cu}_x\text{O}@Z\text{nO}$ combined with US treatment could be an optimal therapeutic modality for CRC treatment.

To reveal the underlying antitumor mechanism of $\text{Cu}_x\text{O}@Z\text{nO}$ (+ US), the piezoelectric and chemodynamic catalytic effects of $\text{Cu}_x\text{O}@Z\text{nO}$ were investigated by quantitating the amounts of intracellular ROS generated by using the probe, 2',7'-dichlorofluorescein diacetate (DCFH-DA). Figure 3C shows that the treatment of PEGylated ZnO and $\text{Cu}_x\text{O}@Z\text{nO}$ produced weak green fluorescence signals in CT-26 cells. Strikingly, upon US exposure, the PEGylated ZnO- and $\text{Cu}_x\text{O}@Z\text{nO}$ -treated cells presented increased green signals. It is worth noting that the $\text{Cu}_x\text{O}@Z\text{nO}$ (+ US)-treated cells displayed the most intense green fluorescence signals, suggesting a synergistically increased production of intracellular ROS by US acting upon the surface coating of Cu_xO (Figure 3D).

Excessive ROS production could cause damage to mitochondrial structures, and to test this hypothesis, mitochondrial membrane integrity was assessed by JC-1 staining for mitochondrial membrane potential.^[25] In the absence of US, weak green fluorescence was observed in the PEGylated ZnO-treated cells, which might be attributed to the generation of a small quantity of intracellular ROS and the minor damage to the mitochondrial structures of CT-26 cells. The $\text{Cu}_x\text{O}@Z\text{nO}$ -treated cells displayed conspicuous green and attenuated red fluorescence due to the synergistic chemodynamic effects of Cu^+ and the toxic effect of Zn^{2+} (Figure 3E). We found that exposure to US further increased the green fluorescence and decreased the red fluorescence. The $\text{Cu}_x\text{O}@Z\text{nO}$ (+ US)-treated cells showed the highest

green and lowest red fluorescence among all cell groups, indicating that $\text{Cu}_x\text{O}@Z\text{nO}$ plus US resulted in the strongest mitochondrial membrane depolarization, thereby confirming the oxidative stress injury.

It is known that increased oxidative stress in tumor cells can lead to their immunogenic cell death (ICD), which is a crucial pathway for promoting dendritic cell (DC) maturation and activating cytotoxic T lymphocytes (CTLs) through the release of biomarker molecules, including calreticulin (CRT), high mobility group protein 1 (HMGB1), and adenosine triphosphate (ATP).^[26,27] As shown in Figure 3F, the control, and the cells only treated with US showed negligible CRT signals. On the contrary, the cells treated with PEGylated ZnO, PEGylated ZnO (+ US), or $\text{Cu}_x\text{O}@Z\text{nO}$ presented prominent CRT signals. It is worth noting that the CRT intensity of the $\text{Cu}_x\text{O}@Z\text{nO}$ (+ US)-treated cells was the strongest among all the groups, which were 11.1-, 1.9-, and 1.9-fold higher than those of the control, PEGylated ZnO (+ US)-, and $\text{Cu}_x\text{O}@Z\text{nO}$ -treated cells, respectively (Figure 3G). Only the treatment of $\text{Cu}_x\text{O}@Z\text{nO}$ (+ US) facilitated the release of nuclear HMGB1, as reflected in the disappearance of the HMGB1 signal (Figure 3F). We found that the $\text{Cu}_x\text{O}@Z\text{nO}$ (+ US)-treated cells exhibited the highest level of extracellular ATP, which was 47.5- and 3.0-fold higher than that observed in the control and $\text{Cu}_x\text{O}@Z\text{nO}$ -treated cells (Figure 3H). These findings support the hypothesis that $\text{Cu}_x\text{O}@Z\text{nO}$ (+ US) is the most effective modality for inducing ICD in colorectal tumor cells.

The glucose transporters (Gluts), particularly Glut1, are commonly overexpressed in most tumor cells due to their high demand for glucose uptake to compensate for inefficient ATP production through anaerobic glycolysis.^[28,29] The downregulation of Glut1 expression to impede glucose transport has been considered a highly productive strategy for inhibiting the progression of tumor cells.^[30] The cellular immunofluorescence staining results revealed that the $\text{Cu}_x\text{O}@Z\text{nO}$ (+ US)-treated cells exhibited a comparatively diminished red fluorescence signal (Glut1) compared to the other groups (Figure S12A,B, Supporting Information). These findings were in agreement with the Western blot results (Figure S12C,D, Supporting Information). The decreased level of Glut1 is expected to benefit from the high-efficacy cell internalization of $\text{Cu}_x\text{O}@Z\text{nO}$ and US treatment. This outcome indicates that $\text{Cu}_x\text{O}@Z\text{nO}$ (+ US) possesses the capability for exceptional reduction in glucose supply.

Glyceraldehyde phosphate dehydrogenase (GAPDH) plays a crucial role in the glycolytic process by catalyzing the dehydrogenation and oxidation of 3-phosphate glyceraldehyde to 1,3-diphosphoglycerate, thereby enabling energy transfer to adenosine diphosphate (ADP) for ATP generation.^[29,31] The relative

Figure 3. In vitro antitumor effect of $\text{Cu}_x\text{O}@Z\text{nO}$ nanoheterojunctions and the corresponding mechanism. A) Relative viabilities of CT-26 cells treated with PEGylated ZnO and $\text{Cu}_x\text{O}@Z\text{nO}$ with or without US. Results were presented as mean \pm S.E.M. ($n = 6$; * $p < 0.05$, ** $p < 0.01$, and *** $p < 0.001$). B) FCM analysis of apoptotic CT-26 cells after treating PEGylated ZnO and $\text{Cu}_x\text{O}@Z\text{nO}$ with or without US. Results were presented as mean \pm S.E.M. ($n = 3$). C,D) Intracellular ROS levels of CT-26 cells and the corresponding MFIs were quantified by Image J software. Scale bar = $20 \mu\text{m}$. E) Mitochondrial membrane potential of CT-26 cells after treating various NPs for 4 h. Scale bar = $20 \mu\text{m}$. F) Expression profiles of CRT and HMGB1 on the surface of CT-26 cells detected by CLSM. G) Quantifying the expression levels of CRT on the surface of CT-26 cells after treating various NPs for 12 h. Scale bar = $20 \mu\text{m}$. H) Released amounts of ATP from CT-26 cells after treating various NPs for 24 h. I) Relative GAPDH mRNA expression levels of CT-26 cells after the treatment of various NPs for 24 h. J) Intracellular ATP amounts of CT-26 cells after treating various NPs for 24 h. K) Relative STING mRNA expression levels of CT-26 cells after the treatment of various NPs for 24 h. Data were presented as mean \pm S.E.M. ($n = 3$; * $p < 0.05$, ** $p < 0.01$ and *** $p < 0.001$). L) Schematic diagram of antitumor mechanism of $\text{Cu}_x\text{O}@Z\text{nO}$ nanoheterojunctions. This figure was created with BioRender.com.

GAPDH mRNA expression level was determined by quantitative real-time polymerase chain reaction (qRT-PCR). We found that treatment with $\text{Cu}_x\text{O}@Z\text{nO}$ (+ US) significantly reduced the relative GAPDH mRNA expression level by 0.8-fold compared to the group without US (Figure 3I), which was confirmed by the Western blot results (Figure S12C,E, Supporting Information). These two indicators demonstrated that $\text{Cu}_x\text{O}@Z\text{nO}$ (+ US) exhibited a non-negligible capacity to decrease Glut1 and GAPDH levels, impairing the glucose supply, inhibiting glycolysis, and ultimately preventing tumor cell progression. In addition, we conducted a quantitative analysis of the intracellular ATP. The $\text{Cu}_x\text{O}@Z\text{nO}$ (+ US)-treated cells had the lowest intracellular ATP content, which was 162.5-fold lower than that of the control and 2.3-fold lower than the $\text{Cu}_x\text{O}@Z\text{nO}$ -treated cells (Figure 3J). These data demonstrate that $\text{Cu}_x\text{O}@Z\text{nO}$ (+ US) possess the most vital capacity to inhibit glucose transport and glycolysis, affecting intracellular ATP production.

The induction of ICD often increases the expression of PD-L1 ligands in tumor cells, attenuating T cell recognition and cytotoxicity against tumor cells through PD-1/PD-L1 interaction.^[32] Consequently, we evaluated the PD-L1 expression level of CT-26 cells with various treatment modalities. It was observed that the surface of the $\text{Cu}_x\text{O}@Z\text{nO}$ (+ US)-treated cells exhibited the most vigorous green fluorescence intensity among all experimental groups (Figure S13A, Supporting Information), indicating that treatment with $\text{Cu}_x\text{O}@Z\text{nO}$ (+ US) promoted PD-L1 expression in CT-26 cells. The FCM results further validated this trend, demonstrating an augmentation in the PD-L1 MFIs of the $\text{Cu}_x\text{O}@Z\text{nO}$ (+ US)-treated cells compared to 1.2- and 1.3-fold increases observed in the PEGylated ZnO (+ US)-treated and $\text{Cu}_x\text{O}@Z\text{nO}$ -treated cells (Figure S13B,C, Supporting Information). Therefore, to increase T-cell recognition of colorectal tumor cells, PD-L1 antibodies ($\alpha\text{PD-L1}$) have been used in in vivo therapeutic investigations.

Tumor-associated macrophages (TAMs) play a pivotal role in tumor immunosuppression.^[33] Specifically, M1-type TAMs secrete substantial quantities of tumor necrosis factor- α (TNF- α) for inhibiting tumor cell growth, facilitating recruitment of CD8⁺ T cells, and attenuating regulatory T-cells (Tregs), thereby stimulating antitumor immune responses.^[34,35] Therefore, we determined the potential of $\text{Cu}_x\text{O}@Z\text{nO}$ (+ US) heterojunctions to induce M1-type macrophage polarization. Compared to the minimal numbers of M1-type macrophages in the control, the control (+ US), and PEGylated ZnO-treated cells, the treatments with PEGylated ZnO (+ US) and $\text{Cu}_x\text{O}@Z\text{nO}$ (\pm US) significantly enhanced the expression of inducible nitric oxide synthase (iNOS, a biomarker of M1-type macrophages) (Figure S14, Supporting Information).^[36] Semi-quantitative analysis of iNOS fluorescence intensities revealed that the combination of $\text{Cu}_x\text{O}@Z\text{nO}$ and US treatment maximized the polarization of M1-type macrophages, exhibiting 6.5-, 3.8-, 1.7-, and 2.4-fold increases compared to the control cells, and those treated with PEGylated ZnO, PEGylated ZnO (+ US), and $\text{Cu}_x\text{O}@Z\text{nO}$.

In addition to antitumor immune activation of ICD, the ROS-induced double-stranded DNA damage-mediated STING signaling pathway is also considered a potent regulator of antitumor immunity.^[37,38] The activation of STING can release some pro-inflammatory cytokines, including interleukin-6 (IL-6) and type

I interferons (IFNs), which facilitate the maturation and activation of immune-related cells, such as DCs, T-cells, and natural killer (NK) cells.^[39–41] Given its importance, we measured the mRNA expression of STING in CT-26 cells subjected to different treatments. Figure 3K revealed that $\text{Cu}_x\text{O}@Z\text{nO}$ nanoheterojunctions exposed to US significantly increased STING mRNA expression, displaying 1.4- and 1.5-fold increases compared to the PEGylated ZnO- and $\text{Cu}_x\text{O}@Z\text{nO}$ -treated cells, respectively. We further benchmarked the critical factors during STING signaling pathway activation at the protein level. It was found that the treatment of $\text{Cu}_x\text{O}@Z\text{nO}$ (+ US) greatly increased the intracellular amounts of STING, P-STING, TANK-binding kinase 1 (TBK1), P-TBK1, interferon regulatory factor 3 (IRF3), and P-IRF3 (Figure S15A–F, Supporting Information). Type I IFNs (e.g., IFN- α and IFN- β) have been recognized as the critical signature cytokines of STING activation,^[42] and TNF- α and CXCL10 are the typical downstream factors of STING pathway.^[43] Thus, their expression levels were determined to confirm the STING activation in CT-26 cells receiving the treatment of $\text{Cu}_x\text{O}@Z\text{nO}$ (+ US). It was observed that $\text{Cu}_x\text{O}@Z\text{nO}$ (+ US) treatment elevated the expression levels of these factors (Figure S15G–J, Supporting Information), suggesting that $\text{Cu}_x\text{O}@Z\text{nO}$ (+ US) successfully activated the STING signaling pathway. The sono-chemodynamic effect and STING activation capacity of $\text{Cu}_x\text{O}@Z\text{nO}$ NPs synergistically induce tumor cell death by impairing mitochondrial function, suppressing glycolysis, triggering ICD, and activating the STING signaling pathway (Figure 3L).

2.4. US Exposure Promotes Colonic Mucus Infiltration and Tumor Penetration of $\text{Cu}_x\text{O}@Z\text{nO}$ NPs

The colonic mucus serves as a formidable barrier against pathogen invasion but also seriously impedes the penetration of therapeutics into the underlying CRC tissues.^[44] The breakthrough of this barrier is critical for optimizing the tumor accumulation of nanotherapeutics.^[45,46] Accordingly, we investigated the penetration profiles of $\text{Cu}_x\text{O}@Z\text{nO}$ nanoheterojunctions with or without US exposure in a simulated colonic mucus fluid containing hydroxyethyl cellulose (HEC, 1.0%, w/v). Figure 4A–D shows the trajectories of $\text{Cu}_x\text{O}@Z\text{nO}$ in the simulated colonic mucus. We observed that US exposure greatly enhanced the movement and mean square displacement (MSD) of $\text{Cu}_x\text{O}@Z\text{nO}$, whereas the absence of US resulted in the immobilization of $\text{Cu}_x\text{O}@Z\text{nO}$ at their original positions. Without the propulsion of US, the $\text{Cu}_x\text{O}@Z\text{nO}$ heterojunctions exhibited a sluggish movement velocity of $0.5 \mu\text{m s}^{-1}$ in the simulated colonic mucus. In contrast, their movement velocity significantly increased to $1.5 \mu\text{m s}^{-1}$ when subjected to US treatment (Figure 4E). Compared to the superficial infiltration distance of $\text{Cu}_x\text{O}@Z\text{nO}$ (100 μm), US-driven $\text{Cu}_x\text{O}@Z\text{nO}$ exhibited a remarkable enhancement in their infiltration capability, extending the distance to 280 μm (Figure 4F). The superior propulsion of $\text{Cu}_x\text{O}@Z\text{nO}$ is primarily attributed to its asymmetric surface, which generates a localized pressure gradient upon exposure to US. This unique characteristic facilitates the penetration of the $\text{Cu}_x\text{O}@Z\text{nO}$ NPs through the colonic mucus barrier and potentially enhances its ability to reach deep CRC tissues.

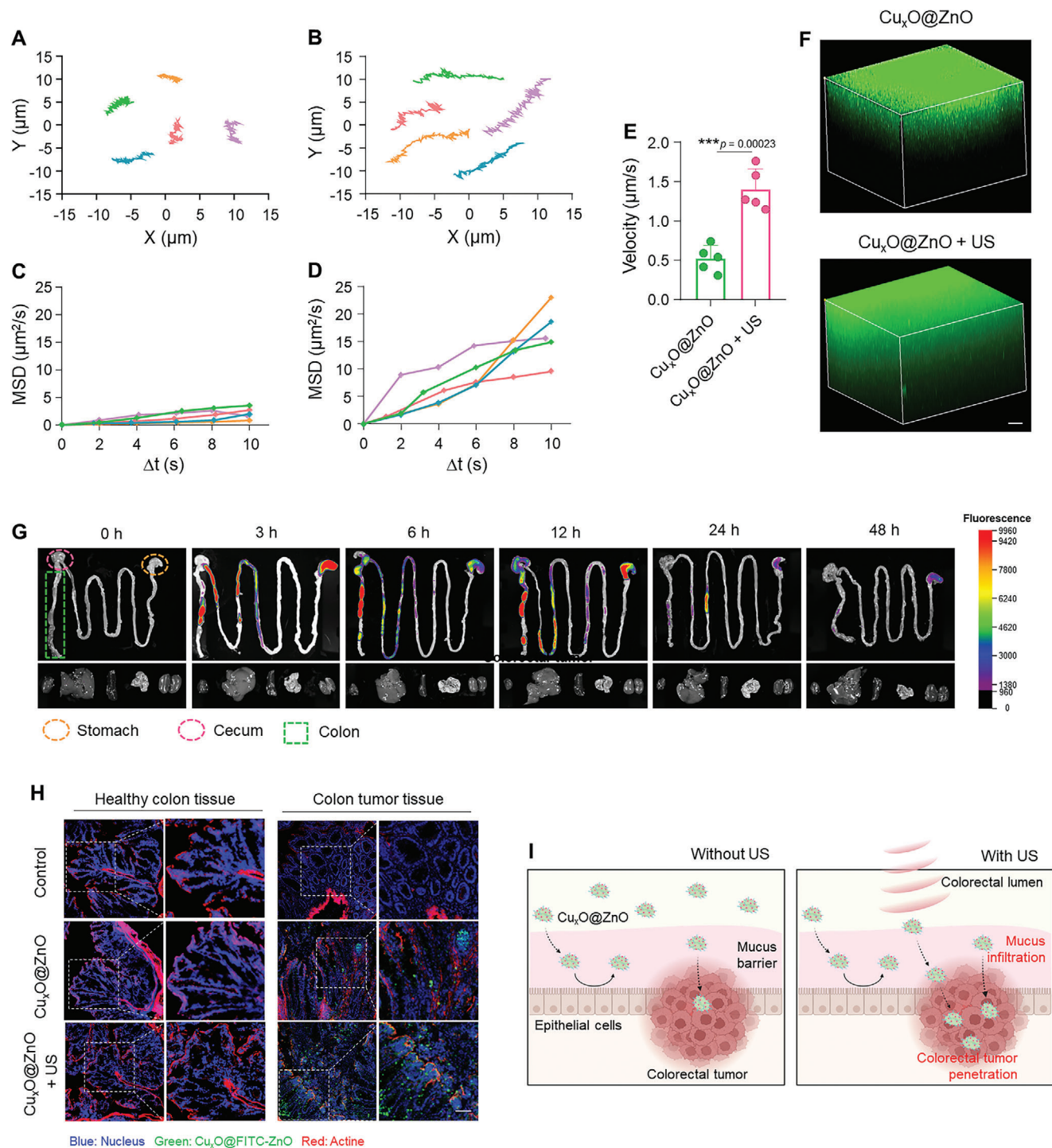


Figure 4. Motion behavior of $\text{Cu}_x\text{O}@Z\text{nO}$ nanoheterojunctions and their accumulation capacity in colorectal tumors. Trajectories (in 10 s) of $\text{Cu}_x\text{O}@Z\text{nO}$ A) without or B) with US. MSDs (in 10 s) of $\text{Cu}_x\text{O}@Z\text{nO}$ C) without or D) with US. E) Motion velocities of $\text{Cu}_x\text{O}@Z\text{nO}$ with or without US. Data are mean \pm S.E.M. ($n = 5$; * $p < 0.05$, ** $p < 0.01$, and *** $p < 0.001$). F) Penetration profiles of $\text{Cu}_x\text{O}@Z\text{nO}$ in the mucus-simulating hydrogels with or without US. G) Fluorescence images of Cy7-labeled $\text{Cu}_x\text{O}@Z\text{nO}$ in the GIT at different time points (0, 3, 6, 12, 24, and 48 h after rectal administration). H) Distribution profiles of $\text{Cu}_x\text{O}@Z\text{nO}$ in the colorectal tumors with or without US. Scale bar = 50 μm . I) Schematic diagram of US-enhanced permeability of $\text{Cu}_x\text{O}@Z\text{nO}$ in the colorectal mucus and tumors. This figure was created with BioRender.com.

Next, we investigated the accumulation of $\text{Cu}_x\text{O}@Z\text{nO}$ NPs in the CRC tissues. $\text{Cu}_x\text{O}@Z\text{nO}$ was covalently labeled with the fluorescent tag (sulfo-cyanine7, Cy7) using 3-aminopropyltriethoxysilane (APTS) as the coupling agent.^[47] Cy7-labeled $\text{Cu}_x\text{O}@Z\text{nO}$ gradually accumulated in the colon lumen as reflected by the intense red fluorescence (Figure 4G). The Cy7 intensity peaked at 12 h after rectal administration, followed by a gradual decline as these NPs were eliminated from the gastrointestinal tract (GIT) (Figure S16, Supporting Information). Five principal organs (heart, lung, liver, kidney, and spleen) were examined at 48 h, and the absence of red fluorescence indicated minimal accumulation of Cy7-labeled $\text{Cu}_x\text{O}@Z\text{nO}$ in these tissues, which avoided the potential for toxicity in these organs. Furthermore, the accumulation profiles of $\text{Cu}_x\text{O}@Z\text{nO}$ NPs in the orthotopic CRC tissues were evaluated through fluorescence staining of cryosections. After rectal administration of FITC-labeled $\text{Cu}_x\text{O}@Z\text{nO}$ nanoheterojunctions, an augmented green fluorescence was observed in the submucosal tumors of US-treated mice compared to those without US treatment (Figure 4H). This observation substantiates the hypothesis that US treatment propels the $\text{Cu}_x\text{O}@Z\text{nO}$ NPs to penetrate both the mucus layer and the colonic epithelial layer, resulting in their preferential accumulation in CRC tumor tissue rather than healthy colon tissue (Figure 4I).

The biosafety of medications has to be tested and ensured to safeguard the healthy tissues from potential damage.^[48] Herein, a panel of indicators evaluated the effects of PBS, $\text{Cu}_x\text{O}@Z\text{nO}$, and $\text{Cu}_x\text{O}@Z\text{nO}$ (+ US) on healthy BALB/c mice at a Zn^{2+} concentration of 5 mg kg⁻¹. The body weights and organ indices of mice treated with $\text{Cu}_x\text{O}@Z\text{nO}$ and $\text{Cu}_x\text{O}@Z\text{nO}$ (+ US) displayed a consistently upward trend, resembling that observed in the PBS control group (Figure S17, Supporting Information), superficially confirming their relative biosafety. The hematological parameters, including white blood cell count (WBC), lymphocyte count (Lymph), and monocyte count (Mon), as well as hepatorenal toxicity markers, such as alkaline phosphatase level (AKP), glutamic oxaloacetic transaminase (AST), alanine aminotransferase (ALT), creatinine (CRE), and blood urea nitrogen (BUN) in the $\text{Cu}_x\text{O}@Z\text{nO}$ (\pm US)-treated groups did not show statistically significant differences compared to those of the PBS control group (Figures S18 and S19, Supporting Information). The H&E-stained sections of the GIT and the five principal organs in the $\text{Cu}_x\text{O}@Z\text{nO}$ (\pm US) groups exhibited histological features indistinguishable from those observed in the PBS control group (Figures S20 and S21, Supporting Information). These findings indicate that $\text{Cu}_x\text{O}@Z\text{nO}$ can efficiently penetrate the mucus layer and rapidly accumulate in the colorectal tumor tissues following rectal administration and exposure to US. This demonstrates the exceptional biocompatibility of the $\text{Cu}_x\text{O}@Z\text{nO}$ (+ US) treatment modality.

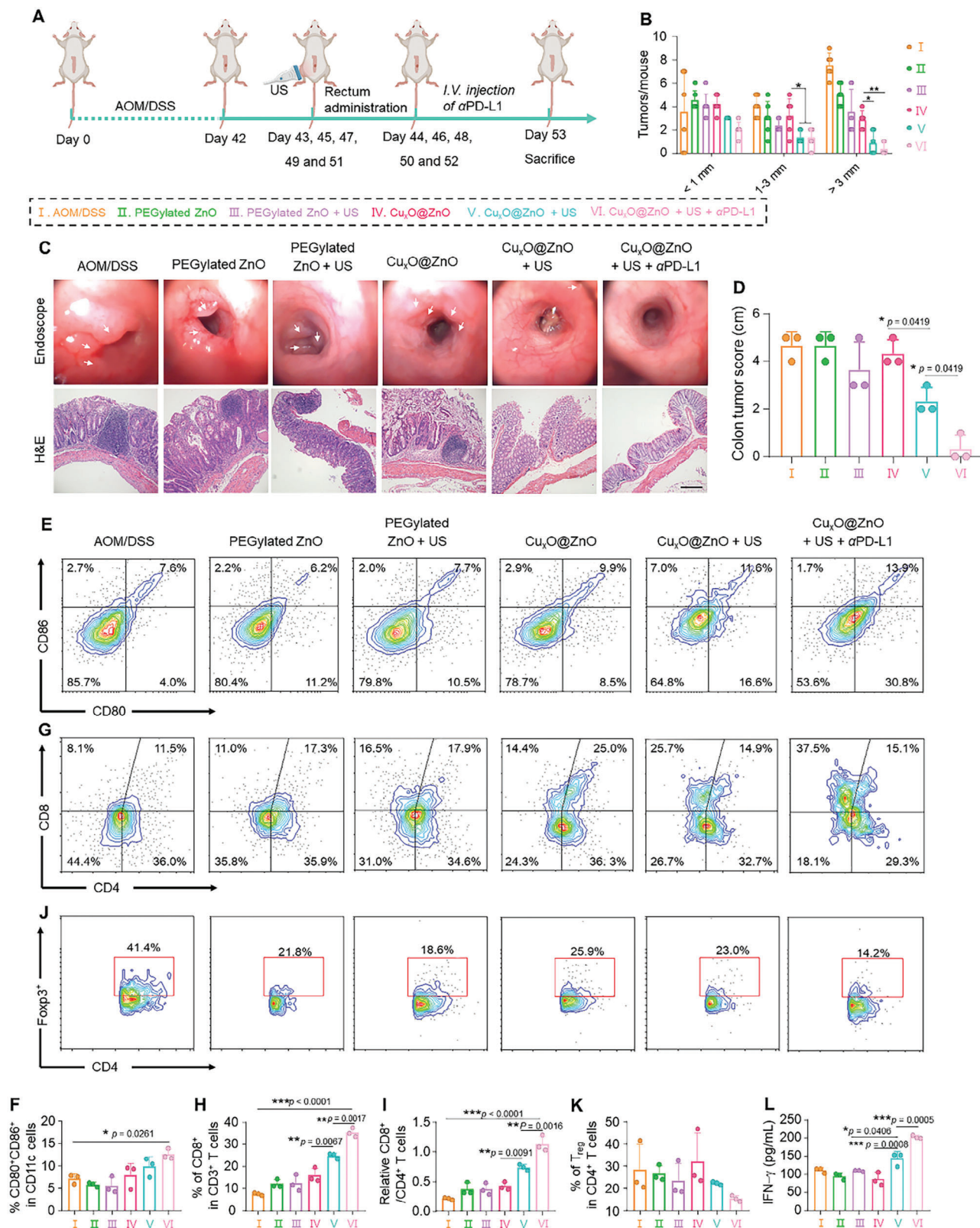
2.5. $\text{Cu}_x\text{O}@Z\text{nO}$ plus US and $\alpha\text{PD-L1}$ Exert a Synergistic Therapeutic Effect Against Orthotopic CRC

The cell experiments revealed that $\text{Cu}_x\text{O}@Z\text{nO}$ plus US treatment activated antitumor immunity by inducing an intense ICD response and activating the STING signaling pathway. And this treatment modality upregulated the expression level of

PD-L1 on the tumor cell membrane. Previous studies demonstrated that blocking the interaction between PD-1 and PD-L1 using $\alpha\text{PD-L1}$ could augment the antitumor immune response by preventing CTL exhaustion, and this strategy has yielded promising clinical treatment outcomes against various cancers.^[49] Therefore, $\alpha\text{PD-L1}$ was employed to enhance the antitumor immunotherapeutic effects of $\text{Cu}_x\text{O}@Z\text{nO}$ plus US treatment.

Initially, we determined the therapeutic effect of $\text{Cu}_x\text{O}@Z\text{nO}$ (+ US + $\alpha\text{PD-L1}$) against CRC as a function of $\text{Cu}_x\text{O}@Z\text{nO}$ amounts (2.5 and 5.0 mg Zn^{2+} per kg mice; 30 μg $\alpha\text{PD-L1}$ per mouse). An orthotopic CRC mouse model was established by injecting CT-26 cells directly into the cecum. As shown in Figure S22 (Supporting Information), $\text{Cu}_x\text{O}@Z\text{nO}$ (+ US + $\alpha\text{PD-L1}$) at a dose of 5.0 mg Zn^{2+} per kg mice almost eliminated the orthotopic colorectal tumors, which presented a stronger anti-CRC effect compared with that at a low Zn^{2+} dosage (2.5 mg Zn^{2+} per kg mice). Therefore, the high dosage (5.0 mg Zn^{2+} per kg mice) was used in the subsequent mouse experiments. After establishing an orthotopic CRC mouse model, a therapeutic procedure was implemented by the protocol outlined in Figure 5A. No discernible weight fluctuations were observed in any of the treatment groups, indicating that these therapeutic modalities had no adverse effects on the expected growth of mice (Figure S23, Supporting Information). The quantification of orthotopic colorectal tumors serves as a visual parameter for evaluating the treatment efficacy of different interventions. We found that the treatments with PEGylated ZnO and $\text{Cu}_x\text{O}@Z\text{nO}$ only reduced the number of large tumors, >3 mm (Figure 5B). Moreover, the $\text{Cu}_x\text{O}@Z\text{nO}$ (+ US)-treated mice exhibited a more significant reduction in the numbers of colorectal tumors compared to the groups receiving treatments with PEGylated ZnO, PEGylated ZnO (+ US), or $\text{Cu}_x\text{O}@Z\text{nO}$. Notably, the combination of $\text{Cu}_x\text{O}@Z\text{nO}$ (+ US) with $\alpha\text{PD-L1}$ showed remarkable reductions in tumor numbers and volumes, confirming its potential as an effective therapy. In addition, the presence of colorectal tumors and colonic mucosal injury were visually assessed through endoscopic examination. It was observed that the $\text{Cu}_x\text{O}@Z\text{nO}$ (+ US + $\alpha\text{PD-L1}$)-treated group presented the smoothest and healthiest colon with the lowest tumor score among all mouse groups (Figure 5C,D). The robust antitumor effectiveness of $\text{Cu}_x\text{O}@Z\text{nO}$, in conjunction with US and $\alpha\text{PD-L1}$, was further validated through H&E staining and analysis of colorectal tumor tissues, characterized by sporadic neoplastic cells (Figure 5C). Conversely, the other groups displayed various numbers of tumor spots. These results demonstrate that this trimodal therapy with $\text{Cu}_x\text{O}@Z\text{nO}$ (+ US + $\alpha\text{PD-L1}$) exhibited optimal therapeutic outcomes against orthotopic CRC.

FCM was utilized to identify the populations of various immune cells to confirm the activation of immunological responses. DCs, as prototypical antigen-presenting cells (APCs), play pivotal roles in innate and adaptive immunities.^[50] Hence, we investigated the maturation profiles of DCs in the thymus in response to various treatment modalities. It was found that the proportions of the activated $\text{CD80}^+\text{CD86}^+$ DCs in the $\text{Cu}_x\text{O}@Z\text{nO}$ (+ US)- and $\text{Cu}_x\text{O}@Z\text{nO}$ (+ US + $\alpha\text{PD-L1}$)-treated groups were significantly higher than those in the control group, with 1.4- and 1.8-fold increases, respectively, indicating their capacity to induce DC maturation (Figure 5E,F) effectively. The



mature DCs present antigens to CD4⁺ T-cells, and the cytokines, such as IFN- γ , from CD4⁺ T-cells regulate the differentiation of CD8⁺ T cells to CTLs and kill tumors. The abundances of CD8⁺ T cells in the colorectal tumor tissues were determined (Figure 5G). The percentage of CD8⁺ T cells in the Cu_xO@ZnO (+ US + α PD-L1)-treated group was the highest (37.4%), with respective increases of 4.6- and 1.5-fold compared to the control group (8.1%) and the Cu_xO@ZnO (+ US)-treated group (25.6%) (Figure 5H). Furthermore, this group exhibited the highest CD8⁺/CD4⁺ T cell ratio (1.13) among all mouse groups, indicating that the combination of Cu_xO@ZnO, US treatment, and α PD-L1 synergistically enhanced antitumor immunity (Figure 5I). These results could be attributed to the activation of antitumor immune responses, enhanced T cell priming through ICD effects, STING activation, and α PD-L1 introduction. The number of regulatory T (Treg) cells responsible for immunosuppression was also determined within colorectal tumors.^[51] The treatment with PEGylated ZnO and Cu_xO@ZnO, with or without US, did not significantly diminish the Treg cell populations in the colorectal tumor tissues. On the contrary, treatment with Cu_xO@ZnO (+ US + α PD-L1) effectively decreased the Treg cell percentage to 15.4%, indicating its strong capacity to reverse the immunosuppressive tumor microenvironment (Figure 5J, K).

Next, we quantified the relative abundance of M1- and M2-phenotype macrophages within the colorectal tumors. Treatment with Cu_xO@ZnO (+ US) and Cu_xO@ZnO (+ US + α PD-L1) remarkably increased the proportions of CD86⁺ cells (M1-type macrophages) by 3.8- and 3.1-fold, respectively, compared to those in the control group (Figure S24A, Supporting Information). Meanwhile, these two treatment groups showed slight decreases in the abundances of CD206⁺ cells (M2-type macrophages), although there was no statistical difference in the percentages of M2-type macrophages among different mouse groups (Figure S24B, Supporting Information). These results support the idea that Cu_xO@ZnO (+ US) significantly facilitates the polarization of macrophages toward the pro-inflammatory M1-type. The levels of the representative inflammatory cytokines (IFN- γ and TNF- α), which are indicative of the antitumor immune response, were measured in the serum.^[52,53] Among all mouse groups, the combination of Cu_xO@ZnO (+ US + α PD-L1) significantly increased the secretion of IFN- γ and TNF- α to 203.1 and 169.6 pg mL⁻¹, respectively. Relative to the Cu_xO@ZnO (+ US)-treated group, the addition of α PD-L1 notably increased the concentrations of IFN- γ and TNF- α by 1.4- and 1.4-fold, respectively (Figure 5L; Figure S25, Supporting Information), suggesting that treatment with Cu_xO@ZnO (+ US + α PD-L1) effectively boosted antitumor immunity. Consequently, sonodynamic Cu_xO@ZnO plus α PD-L1 demonstrated a potent antitumor ef-

fect, ascribed to generating abundant intracellular ROS and eliciting immunological responses.

Gut microbiota is essential in the physiological processes of nutrient absorption, mucosal barrier integrity maintenance, and intestinal immunity regulation.^[54] Their dysbiosis is closely associated with the occurrence and progression of CRC.^[55] The intestinal microbiota from various mouse groups was analyzed through 16S rRNA sequencing. The α -diversity of the gut microbiota, as measured by Sobs (Figure 6A), Chao (Figure 6B), and Shannon (Figure 6C) indices at the operational taxonomic unit (OTU) level, demonstrated obvious increases in the Cu_xO@ZnO (+ US)- and Cu_xO@ZnO (+ US + α PD-L1)-treated groups, in comparison with those in the azoxymethane (AOM)/dextran sulfate sodium salt (DSS) control group. This result suggests that these interventions have promising implications for augmenting microbial richness and diversity. Principal coordinates analysis (PCoA) based on Bray-Curtis distance revealed an apparent differentiation in the gut microbiota populations between the AOM/DSS control group and the Cu_xO@ZnO (+ US \pm α PD-L1)-treated groups (Figure 6D). The Venn diagram illustrates a total of 82 species shared among all groups, while the numbers of unique species in the AOM/DSS control, PEGylated ZnO-, PEGylated ZnO (+ US)-, Cu_xO@ZnO-, Cu_xO@ZnO (+ US)-, and Cu_xO@ZnO (+ US + α PD-L1)-treated groups were 16, 17, 6, 7, 24, and 18, respectively (Figure 6E). The total species numbers exhibited significant increases after treatment with Cu_xO@ZnO (+ US) and Cu_xO@ZnO (+ US + α PD-L1), which were 1.3- and 1.3-fold higher than the AOM/DSS control group. These results further validate their efficacy in increasing the abundance of intestinal microbes.

The phylum-level analysis revealed an imbalance in the abundance of *Firmicutes* in the AOM/DSS control, PEGylated ZnO-, and Cu_xO@ZnO-treated groups. However, the US- or α PD-L1-treated groups exhibited noticeable *Firmicute* reductions (Figure 6F). We found that mouse groups receiving treatments with Cu_xO@ZnO (+ US) and Cu_xO@ZnO (+ US + α PD-L1) presented increased abundances of *Bacteroidetes* and *Actinobacteria*, underscoring the efficacy of multi-modal therapy in modulating the intestinal microbiota balance. This phenomenon might be ascribed to the direct and indirect regulation of colorectal immune immunoenvironment, microbiota derivatives, and microbiota circuits by nanomedicines. The species composition and relative abundance of gut microbiota following different treatments at the genus level were also determined. Disparities in the abundance of beneficial bacteria, such as *Alistipes*,^[56] *Bifidobacterium*,^[57] *Muribaculaceae*,^[58] and *Odoribacteraceae*,^[59] and detrimental bacteria like *Romboutsia* strains^[60] were observed across each group (Figure 6G). Interestingly, all US-executed treatments elevated

Figure 5. In vivo therapeutic outcomes of Cu_xO@ZnO nanoheterojunctions against orthotopic CRC. A) Schematic illustration of the treatment protocol of Cu_xO@ZnO against orthotopic CRC. B) Tumor size distributions per mouse. Data are mean \pm S.E.M. ($n = 6$; * $p < 0.05$, ** $p < 0.01$, and *** $p < 0.001$). C) Endoscopic images of colorectal tumor and H&E staining of colorectal tumor tissue sections from various mouse groups. Scale bar = 200 μ m. D) Endoscopic scores of the colorectal tumors from various mouse groups. Data are mean \pm S.E.M. ($n = 3$; * $p < 0.05$, ** $p < 0.01$, and *** $p < 0.001$). E) Representative FCM images of DCs (CD80⁺CD86⁺) gated on CD11c⁺ DCs in the thymuses from various mouse groups. F) Percentages of DCs in the thymuses from various mouse groups. G) Representative FCM images of CD4⁺ and CD8⁺ T-cells (gated on CD45⁺CD3⁺ T-cells) in the orthotopic colorectal tumors from various mouse groups. H) Percentages of CD8⁺ T-cells in the orthotopic colorectal tumors from various mouse groups. I) The ratio of CD8⁺/CD4⁺ T-cells in the orthotopic colorectal tumors. J) Representative FCM images of Tregs (gated on CD4⁺ T-cells) in the orthotopic colorectal tumors from various mouse groups. K) Quantification of Tregs (CD4⁺Foxp3⁺) in the orthotopic colorectal tumors. L) IFN- γ amounts in the serum from various mouse groups. Data are mean \pm S.E.M. ($n = 3$; * $p < 0.05$, ** $p < 0.01$, and *** $p < 0.001$).



Figure 6. Regulation of gut microbiota composition of $\text{Cu}_x\text{O}@Zn\text{O}$ under US. A-C) α -Diversity (Sobs, Chao, and Shannon indexes) analysis on the OTU level of microbiota from various mouse groups. D) β -Diversity (PCoA) analysis of microbiota (OTU level) from various mouse groups. E) Venn diagram of microbiota (OTU level) and histogram of the total species number of microbiota from various mouse groups. F) Species composition of gut microbiota at the phylum level of various mouse groups. G) Species composition of gut microbiota at the genus level of various mouse groups. H–L) Relative abundance of microbiota negatively associated with CRC (*Alistipes*, *Bifidobacterium*, *Muribaculaceae*, and *Odoribacteraceae*) and positively associated with CRC (*Romboutsia*) at the genus level in various mouse groups. Data are mean \pm S.E.M. ($n = 3$; * $p < 0.05$, ** $p < 0.01$, and *** $p < 0.001$).

the abundance of beneficial bacteria that were inversely associated with CRC development, while simultaneously reducing the prevalence of harmful bacteria that were positively linked to CRC (Figure 6H–L). For example, the average abundances of *Alistipes*, *Bifidobacterium*, *Muribaculaceae*, and *Odoribacteraceae* were increased by 34.0-, 20.6-, 87.5-, and 3.7-fold in the $\text{Cu}_x\text{O}@Zn\text{O}$ (+ US + $\alpha\text{PD-L1}$)-treated group, respectively, in comparison with the AOM/DSS control group. The treatment of $\text{Cu}_x\text{O}@Zn\text{O}$ (+ US + $\alpha\text{PD-L1}$) remodeled the imbalanced microbiota toward a healthy microbiota, which was presented in our previous reports.^[46,61] These findings suggest that the combination of US-activated

$\text{Cu}_x\text{O}@Zn\text{O}$ plus $\alpha\text{PD-L1}$ holds great promise for effectively managing CRC by modulating the gut microbiota balance associated with its progression.

2.6. $\text{Cu}_x\text{O}@Zn\text{O}$ Plus US activation and $\alpha\text{PD-L1}$ Exert Synergistic Therapeutic Effects against Orthotopic and Distant CRC

In this series of experiments, we aimed to assess the potential of $\text{Cu}_x\text{O}@Zn\text{O}$ plus US treatment and $\alpha\text{PD-L1}$ to activate

antitumor immunity, induce immunological memory responses, and inhibit distant colorectal tumors. After evaluating the treatment efficacies of $\text{Cu}_x\text{O}@Z\text{nO}$ (+ US) and $\text{Cu}_x\text{O}@Z\text{nO}$ (+ US + $\alpha\text{PD-L1}$) against orthotopic CRC, we inoculated CT-26 cells on the dorsal region of mice to establish a distant tumor model (Figure 7A). Mouse body weights and distant tumor volumes were recorded on alternate days. As shown in Figure S26 (Supporting Information), mice in all groups behaved usually, with no observed abnormal weight loss, thereby substantiating the absence of any apparent systemic toxicity. The successful suppression of orthotopic tumors was reconfirmed by $\text{Cu}_x\text{O}@Z\text{nO}$ (+ US) treatment, especially when combined with $\alpha\text{PD-L1}$ (Figure 7B). The distant tumor growth results demonstrated an uncontrolled escalating pattern in the AOM/DSS control group. Conversely, the treatment of $\text{Cu}_x\text{O}@Z\text{nO}$ (+ US) effectively inhibited the growth of distant tumors (Figure 7C,D). Remarkably, the combination of $\text{Cu}_x\text{O}@Z\text{nO}$ (+ US + $\alpha\text{PD-L1}$) achieved synergistic inhibitory efficacy in controlling the volumes of distant tumors below 63.2 mm^3 , possibly due to memory T cells (Figure 7E). Figure 7F indicated that the $\text{Cu}_x\text{O}@Z\text{nO}$ (+ US + $\alpha\text{PD-L1}$)-treated group had the lowest tumor weight (14.7 mg), which was 5.1- and 2.9-fold lower compared to the AOM/DSS control and $\text{Cu}_x\text{O}@Z\text{nO}$ (+ US)-treated groups, respectively. The necrosis and apoptosis of distant tumors were further evaluated using H&E and TUNEL staining.^[62] As shown in Figure 7G, the distant tumors in the AOM/DSS control group showed almost no necrotic or apoptotic cells; conversely, a noticeable appearance of necrosis and apoptosis within the tumors was observed in the $\text{Cu}_x\text{O}@Z\text{nO}$ (+ US)-treated group. Notably, the extent of necrosis and apoptosis in the distant tumors was enhanced by treatment with $\text{Cu}_x\text{O}@Z\text{nO}$ (+ US + $\alpha\text{PD-L1}$), as evidenced by the sparse distribution of tumor cells and the substantial area of green fluorescent apoptotic cells (Figure 7H). These outcomes suggest that $\text{Cu}_x\text{O}@Z\text{nO}$ (+ US + $\alpha\text{PD-L1}$) not only shows a direct anti-CRC effect through ROS generation but also significantly elicits an immunological memory response to impede the proliferation of distant tumor cells.

To intuitively evaluate the effectiveness of $\text{Cu}_x\text{O}@Z\text{nO}$ (+ US + $\alpha\text{PD-L1}$) in inducing antitumor immunological memory responses, we measured the percentages of typical immune cells, such as CTLs, central memory T-cells (CMTs), and effector memory T-cells (EMTs) in the distant tumors and spleens following various treatments.^[63,64] Immunofluorescence staining of the distant tumor tissues revealed that treatment with $\text{Cu}_x\text{O}@Z\text{nO}$ (+ US) and $\text{Cu}_x\text{O}@Z\text{nO}$ (+ US + $\alpha\text{PD-L1}$) enhanced the infiltration of CD4^+ and CD8^+ T-cells, while concurrently suppressing the expansion of immunosuppressive Treg cells (Foxp3^+), in comparison with the AOM/DSS control group (Figure 7I; Figure S27A, Supporting Information). Based on the semi-quantitative analyses, we concluded that the abilities to activate the CD4^+ and CD8^+ T cells and inhibit the expansion of Treg cells were the strongest. Compared with the AOM/DSS control and $\text{Cu}_x\text{O}@Z\text{nO}$ (+ US)-treated groups, the levels of CD4^+ and CD8^+ T-cells were significantly increased by 2.3- as well as 1.5-fold, and 2.2- as well as 1.8-fold, respectively, in response to the treatment with $\text{Cu}_x\text{O}@Z\text{nO}$ (+ US + $\alpha\text{PD-L1}$) (Figure 7J,K). In contrast, these two groups showed 3.9- and 2.9-fold reductions in the Treg cell levels (Figure S27B, Supporting Information). Interestingly, rectal administration of $\text{Cu}_x\text{O}@Z\text{nO}$ (+ US + $\alpha\text{PD-L1}$)

also significantly augmented the proportions of CD4^+ T-cells and CD8^+ T cells in the spleen, as evidenced by FCM results. The combination of $\text{Cu}_x\text{O}@Z\text{nO}$ with US and $\alpha\text{PD-L1}$ significantly increased the percentage of CD8^+ T cells to 14.3%, exhibiting remarkable 1.8- and 1.5-fold increases compared to the AOM/DSS control and $\text{Cu}_x\text{O}@Z\text{nO}$ (+ US)-treated groups (Figure 7L, M). The implementation of $\text{Cu}_x\text{O}@Z\text{nO}$ (+ US) in conjunction with $\alpha\text{PD-L1}$ also facilitated the transition of CMT within the CD8^+ T cell population into EMT ($\text{CD44}^+\text{CD62L}^-$) (Figure 7N). Similarly, the $\text{Cu}_x\text{O}@Z\text{nO}$ (+ US + $\alpha\text{PD-L1}$)-treated group showed an elevated level of CD4^+ T cells (26.9%) compared with the remaining groups (Figure 7O, P). In contrast to the results on CD8^+ T-cells, treating $\text{Cu}_x\text{O}@Z\text{nO}$ (+ US + $\alpha\text{PD-L1}$) promoted the differentiation of naïve cells within the CD4^+ T cell population toward CMT and EMT subsets (Figure 7Q). The activation of EMT exerted a crucial inhibitory effect against distant tumors.

3. Conclusion

A novel flying-saucer-shaped nanoheterojunction was fabricated by applying copper oxide (Cu_xO) on the surface of PEGylated zinc oxide (ZnO) for the synergistic treatment of colorectal cancer. This sonodynamic therapy strategy, powered by ultrasound energy, enormously improved the recombination of electron-hole pairs in the PEGylated ZnO band structure, suppressed the rapid recombination of electron-hole pairs, and ultimately led to band bending, which significantly promoted the generation of antitumor reactive oxygen species. The Cu_xO with Cu^+ also exhibited a Fenton-like reaction that utilized abundant intracellular hydrogen peroxide to generate hydroxyl radicals. This sonodynamic and chemodynamic therapeutic platform, in combination with $\alpha\text{PD-L1}$, showed excellent inhibitory activities against orthotopic and distant colorectal tumors through the activation of systemic antitumor immunity, the regulation of glucose metabolism in tumor cells, and the rebalancing of intestinal microbiota toward beneficial species.

4. Experimental Section

Synthesis of PEGylated ZnO: PEG (MW = 8000 Da) (1 g) and anhydrous ethanol (97 mL) were introduced into a 100 mL round bottom flask, followed by heating and stirring in an oil bath at $80\text{ }^\circ\text{C}$ to form a PEG solution. The above solution was subsequently treated with a rapid addition of 3 mL of zinc acetate ($\text{Zn}(\text{Ac})_2$), and the reaction was allowed to proceed for 2 h. Following cooling to room temperature, the solution was centrifuged (8000 g, 5 min) and washed twice with H_2O to collect PEGylated ZnO.

Synthesis of Cu_xO : Cu_xO NPs were synthesized following a previously reported method. Briefly, copper chloride (CuCl_2) powders (33.6 mg) were dissolved in H_2O (25 mL) and subjected to magnetic stirring for 10 min at a temperature of $80\text{ }^\circ\text{C}$ in an oil bath. The L-ascorbic acid (AA) aqueous solution (100 mM, 25 mL) was slowly added to the CuCl_2 solution. After that, the pH value of the solution was adjusted to 8.0–9.0 by adding sodium hydroxide (NaOH) solution (1.0 M), which was maintained at a temperature of $80\text{ }^\circ\text{C}$ for an additional 12 h reaction with continuous stirring. After the response, the large aggregates were eliminated through centrifugation at 5,438 g for 15 min. Subsequently, the resulting supernatant was dialyzed against H_2O (with a molecular weight cutoff of 10000 Da) for 2 days. The purified Cu_xO suspension was stored in a refrigerator at $4\text{ }^\circ\text{C}$.

Fabrication of $\text{Cu}_x\text{O}@Z\text{nO}$ Nanoheterojunctions: Briefly, the PEGylated ZnO suspension (Zn : $500\text{ }\mu\text{g mL}^{-1}$, 1 mL) was added dropwise to the Cu_xO solution (Cu : $21.7\text{ }\mu\text{g mL}^{-1}$, 4 mL), which was stirred for 2 h at

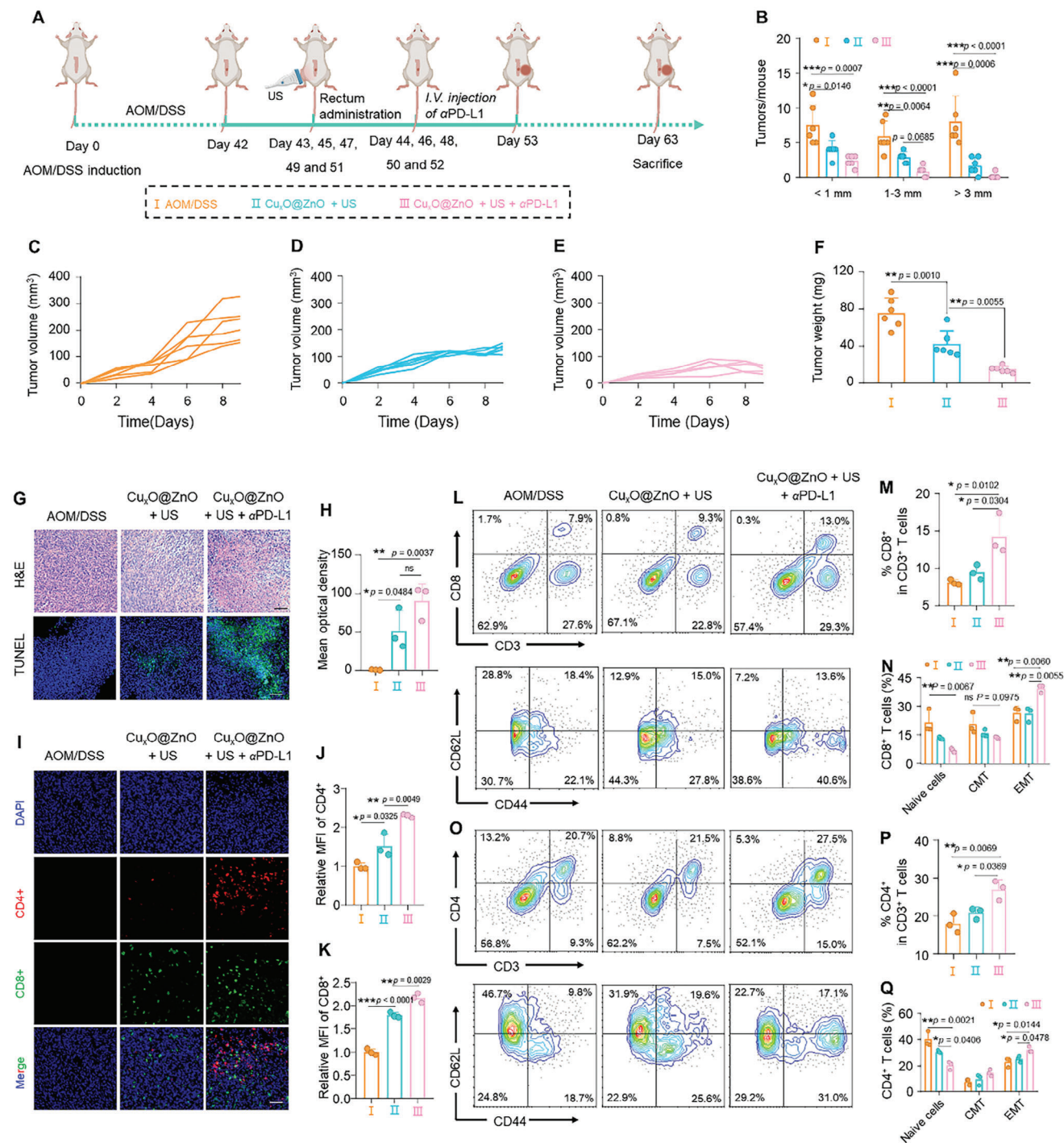


Figure 7. Long-term immune-memory effects induced by $\text{Cu}_2\text{O}@Z\text{nO}$ under US. A) Schematic illustration of $\text{Cu}_2\text{O}@Z\text{nO}$ (+ US) and $\alpha\text{PD-L1}$ combination therapy to inhibit distant tumor. B) Primary tumor size distributions per mouse. Data are mean \pm S.E.M. ($n = 6$; $^*p < 0.05$, $^{**}p < 0.01$, and $^{***}p < 0.001$). Distant tumor growth curves of the C) control, D) $\text{Cu}_2\text{O}@Z\text{nO}$ (+ US), and E) $\text{Cu}_2\text{O}@Z\text{nO}$ (+ US + $\alpha\text{PD-L1}$) groups. F) Distant tumor weights of various mouse groups. Data are mean \pm S.E.M. ($n = 6$; $^*p < 0.05$, $^{**}p < 0.01$, and $^{***}p < 0.001$). G) H&E and TUNEL staining images of distant tumors from various mouse groups. Scale bar = 100 μm . H) Mean optical density analysis of TUNEL staining for various mouse groups. Data are mean \pm S.E.M. ($n = 3$; $^*p < 0.05$, $^{**}p < 0.01$, and $^{***}p < 0.001$). I-K) Representative CLSM images and MFIs of CD4^+ and CD8^+ T-cells in the distant tumors (Scale bar = 50 μm). L) Representative FCM images of splenic lymphocytes in the distant tumor model from various mouse groups (gated on $\text{CD3}^+\text{CD8}^+$ T-cells). M, N) Percentages of CD8^+ T-cells, naive T-cells, CMT, and EMT in the spleens from various mouse groups. Statistical significances were calculated via one-way analysis of variance (ANOVA) followed by Tukey's post hoc test ($n = 3$; $^*p < 0.05$, $^{**}p < 0.01$, and $^{***}p < 0.001$). O) Representative FCM images of splenic lymphocytes in the distant tumors from various mouse groups (gated on $\text{CD3}^+\text{CD4}^+$ T-cells). P, Q) Percentages of CD4^+ T-cells, naive T cells, CMT, and EMT in the spleens from various mouse groups. Statistical significances were calculated via one-way analysis of variance (ANOVA) followed by Tukey's post hoc test ($n = 3$; $^*p < 0.05$, $^{**}p < 0.01$, and $^{***}p < 0.001$).

room temperature. After centrifugation at 8 000 *g* for 10 min, the resultant composite NPs (Cu_xO@ZnO) were collected, subjected to two rounds of washing, and stored at 4 °C for future applications.

In Vitro Cytotoxicity of NPs: The cytotoxicity of PEGylated ZnO and Cu_xO@ZnO was evaluated using MTT assay. Initially, CT-26 and L929 cells were seeded separately in 96-well culture plates at a density of 1 × 10⁴ cells per well and incubated overnight at 37 °C. Subsequently, PEGylated ZnO and Cu_xO@ZnO suspensions at the Zn²⁺ concentrations of 0.5, 1, 2, 4, 6, and 8 μg mL⁻¹ were co-incubated with CT-26 and L929 cells. After co-incubation for 4 h, cells in the US-involved groups were subjected to sonodynamic treatment (1.0 MHz, 1.0 W cm⁻²) for 1 min, after which they were cultured for an additional 20 h. The viabilities of CT-26 and L929 cells receiving different treatments were detected using MTT reagent on a microplate reader (SYNERGY/H1, Bio Tek, Vermont, US).

mRNA Expression Levels of GAPDH and STING: CT-26 cells were seeded in 12-well plates at a density of 2 × 10⁵ per well and cultured overnight. Subsequently, the complete media were replaced with PEGylated ZnO or Cu_xO@ZnO suspensions at a Zn²⁺ concentration of 6 μg mL⁻¹. After 4 h of cultivation, the cells in the US-involved groups were subjected to US exposure (1.0 MHz, 1.0 W cm⁻²) for 1 min and cultured for an additional period of 20 h. Cells were collected through trypsin digestion and centrifugation (400 *g*, 5 min). The total mRNA was extracted from these cells using a Trizol reagent after amplifying cDNA on a real-time PCR machine (Thermo Fisher Scientific, Applied Biosystems QuantStudio3, Massachusetts, US) to detect the mRNA expression levels of GAPDH and STING.

In Vivo Therapeutic Outcomes of NPs Against Orthotopic Colorectal Cancer: Mice with orthotopic colorectal tumors were randomly divided into six groups (*n* = 6), namely: 1) AOM/DSS control, 2) PEGylated ZnO, 3) PEGylated ZnO (+ US), 4) Cu_xO@ZnO, 5) Cu_xO@ZnO (+ US), and 6) Cu_xO@ZnO (+ US + αPD-L1). Mice were rectally administrated with various NPs (Zn²⁺, 5 mg kg⁻¹) every 2 days. After rectal administration, the US-involved groups received US (frequency: 1.0 MHz, intensity: 1.0 W cm⁻², duration: 5 min). Mouse body weights were recorded at 2-day intervals throughout the entire process. At the end of the experiments, colorectal tumor images were obtained through endoscopy (Yuyan instrument, YAN-E30, Shanghai, China). The colons and major organs (heart, liver, spleen, lung, and kidney) were subjected to H&E staining. The DCs were isolated from the thymus and subjected to FCM analysis after co-staining with anti-mouse CD11c-FITC (Catalog: 117306), anti-mouse CD80-APC/Fire 750 (Biolegend, Catalog: 104740), and anti-mouse CD86-PE (Biolegend, Catalog: 159204) for quantification of DC maturation. T-cell phenotypes and macrophages were isolated from colon tissues and stained for detection of CD4⁺/CD8⁺ T-cell activation as well as Treg cell suppression using the following antibodies: anti-CD45-APC-Cy7 (Biolegend, Catalog: 103116), anti-CD3-APC (Biolegend, Catalog: 100236), anti-CD4-FITC (Biolegend, Catalog: 100405), anti-CD8a-PerCP-Cy5.5 (Biolegend, Catalog: 100734), anti-Foxp3-PE (Biolegend, Catalog: 126404), anti-F4/80-PerCP (Biolegend, Catalog: 123126), anti-CD86-PE (Biolegend, Catalog: 159204, and anti-CD206-APC (Biolegend, Catalog: 141708) based on FCM (CYTOFLEX, Beckman Coulter, California, US). Meanwhile, blood samples were collected to quantify serum pro-inflammatory cytokines, including TNF-α and IFN-γ, using the corresponding ELISA kits (Solarbio Science & Technology Co., Ltd., Beijing, China).

In Vivo Therapeutic Outcomes of NPs Against Orthotopic and Distant Colorectal Tumors: Following the completion of treatments in mice with orthotopic colorectal tumors, including 1) AOM/DSS, 2) Cu_xO@ZnO (+ US), and 3) Cu_xO@ZnO (+ US + αPD-L1), CT-26 cells (3 × 10⁶ cells, 200 μL) were subcutaneously injected into the right flanks of mice to establish a mouse model with both orthotopic and distant colorectal tumors. The volumes of distant tumors were measured every 2 days to record the tumor growth. After a 10-day monitoring period, distant tumors were collected, dissected, and subjected to histological examination using H&E and TUNEL staining. Additionally, immunofluorescence staining was performed to evaluate immune cell markers (CD4, CD8, and Foxp3). The spleen was excised to obtain a single-cell suspension for quantifying memory and effector T-cell phenotypes. Subsequently, cells were stained with anti-CD3-FITC (Biolegend, Catalog: 100204), anti-CD4-PerCP-Cy5.5

(Biolegend, Catalog: 100407), anti-CD8a-PerCP-Cy5.5 (Biolegend, Catalog: 100732), anti-CD44-APC (Biolegend, Catalog: 103012), and anti-CD62L-PE (Biolegend, Catalog: 104407) antibodies for FCM analysis.

Statistical Analysis: The experiments were conducted with technical replicates, and the data were calculated and presented as mean ± standard error of the mean (S.E.M.), unless otherwise specified. Investigators were blinded to group allocation during experiments. The specific statistical methods are defined in the figure legends. Statistical differences between the two groups were assessed using a two-tailed Student's *t*-test. Comparisons among more than three groups were conducted through a one-way analysis of variance (ANOVA) followed by Tukey's post hoc test. The threshold for statistical significance was set at *p* < 0.05 for all tests. Additionally, significance levels were denoted as **p* < 0.05, ***p* < 0.01, and ****p* < 0.001, and ns indicates no significant difference. All statistical analyses were conducted using GraphPad Prism 8.0 and Origin 2018.

Supporting Information

Supporting Information is available from the Wiley Online Library or from the author.

Acknowledgements

This study was supported by the National Natural Science Foundation of China (82072060, 82360110, and 22008201), the Fundamental Research Funds for the Central Universities (SWU-XDPY22006 and SWU-KQ22075), the Venture & Innovation Support Program for Chongqing Overseas Returnees (2205012980212766), and the Distinguished Young Scholars of Chongqing (2022NSCQ-JQX5279).

Conflict of Interest

The authors declare that they have no competing interests.

Author Contributions

X.S., Z.L., and B.X. performed the experiments, supervised the project, and wrote the manuscript draft. Y.M., Y.C., M.Z., Q.G., G.L., J.J., H.X., and Q.Y. performed the experiments. Y.M., X.S., R.R., S.K., J.Z., Z.L., and B.X. edited and revised the manuscript. S.C. Kundu wishes to express his sincere thanks for supporting him with facilities by the Southwest University for the collaborative research visit at the State Key Laboratory of Resource Insects. All authors approved the final version of the manuscript.

Data Availability Statement

The data supporting this study's findings are available from the corresponding author upon reasonable request.

Keywords

colorectal cancer, immunotherapy, microbiota metabolite regulation, nanoheterojunction, tumor accumulation

Received: February 3, 2024

Revised: June 20, 2024

Published online: July 2, 2024

[1] S. Son, J. H. Kim, X. Wang, C. Zhang, S. A. Yoon, J. Shin, A. Sharma, M. H. Lee, L. Cheng, J. Wu, J. S. Kim, *Chem. Soc. Rev.* **2020**, *49*, 3244.

- [2] J. Liang, X. Qiao, L. Qiu, H. Xu, H. Xiang, H. Ding, Y. Chen, *Adv. Sci.* **2024**, *11*, 2305392.
- [3] P. Wang, Q. Tang, L. Zhang, M. Xu, L. Sun, S. Sun, J. Zhang, S. Wang, X. Liang, *ACS Nano* **2021**, *15*, 11326.
- [4] J. Ouyang, Z. Tang, N. Farokhzad, N. Kong, N. Y. Kim, C. Feng, S. Blake, Y. Xiao, C. Liu, T. Xie, W. Tao, *Nano Today* **2020**, *35*, 100949.
- [5] Q. Wang, Y. Tian, M. Yao, J. Fu, L. Wang, Y. Zhu, *Adv. Mater.* **2023**, *35*, 2301784.
- [6] X. Qian, Y. Zheng, Y. Chen, *Adv. Mater.* **2016**, *28*, 8097.
- [7] Y. Zhao, S. Wang, Y. Ding, Z. Zhang, T. Huang, Y. Zhang, X. Wan, Z. L. Wang, L. Li, *ACS Nano* **2022**, *16*, 9304.
- [8] R. Zhang, D. Yang, P. Pang, F. He, S. Gai, Y. Kuang, G. Yang, P. Yang, *Adv. Mater.* **2023**, *36*, 2308355.
- [9] Z. Feng, X. Xiang, J. Huang, L. Wang, B. Zhu, H. Zhou, H. Pang, C. Cheng, L. Ma, L. Qiu, *Adv. Funct. Mater.* **2023**, *33*, 2302579.
- [10] X. Yuan, Y. Kang, J. Dong, R. Li, J. Ye, Y. Fan, J. Han, J. Yu, G. Ni, X. Ji, D. Ming, *Nat. Commun.* **2023**, *14*, 5140.
- [11] Y. Liao, D. Wang, S. Zhu, R. Zhou, F. Rahbarizadeh, Z. Gu, *Nano Today* **2022**, *44*, 101510.
- [12] C. Pan, M. Ou, Q. Cheng, Y. Zhou, Y. Yu, Z. Li, F. Zhang, D. Xia, L. Mei, X. Ji, *Adv. Funct. Mater.* **2020**, *30*, 1906466.
- [13] Q. Xu, X. Gao, S. Zhao, Y. N. Liu, D. Zhang, K. Zhou, H. Khanbareh, W. Chen, Y. Zhang, C. Bowen, *Adv. Mater.* **2021**, *33*, 2008452.
- [14] J. W. Rasmussen, E. Martinez, P. Louka, D. G. Wingett, *Expert Opin. Drug Delivery* **2010**, *7*, 1063.
- [15] S. Anjum, M. Hashim, S. A. Malik, M. Khan, J. M. Lorenzo, B. H. Abbasi, C. Hano, *Cancers* **2021**, *13*, 4570.
- [16] Q. T. Hoang, V. Ravichandran, T. G. Nguyen Cao, J. H. Kang, Y. T. Ko, T. I. Lee, M. S. Shim, *Chem. Eng. J.* **2022**, *435*, 135039.
- [17] Y. Zhang, S. Wang, Y. Zhao, Y. Ding, Z. Zhang, T. Jiang, Z. L. Wang, L. Li, *Mater. Today Nano* **2022**, *18*, 100177.
- [18] T. R. Gurugubelli, R. V. S. S. N. Ravikumar, R. Koutavarapu, *Catalysts* **2022**, *12*, 84.
- [19] T. Hu, F. Li, K. Yuan, Y. W. Chen, *ACS Appl. Mater. Interfaces* **2013**, *5*, 5763.
- [20] W. Huang, D. Bai, L. Li, H. Wei, Z. Shi, H. Cheng, Y. Q. Li, *J. Sol-gel. Sci. Technol.* **2015**, *74*, 718.
- [21] X. Xing, S. Zhao, T. Xu, L. Huang, Y. Zhang, M. Lan, C. Lin, X. Zheng, P. Wang, *Coordin. Chem. Rev.* **2021**, *445*, 214087.
- [22] Q. T. Hoang, D. Y. Kim, H. S. Park, W. Jang, T. G. Nguyen Cao, J. H. Kang, Y. T. Ko, S. J. Mun, S. H. Bhang, M. S. Shim, K. W. Bong, *Adv. Funct. Mater.* **2024**, *34*, 2306078.
- [23] L. S. Lin, J. F. Wang, J. Song, Y. Liu, G. Zhu, Y. Dai, Z. Shen, R. Tian, J. Song, Z. Wang, W. Tang, G. Yu, Z. Zhou, Z. Yang, T. Huang, G. Niu, H. H. Yang, Z. Y. Chen, X. Chen, *Theranostics* **2019**, *9*, 7200.
- [24] Y. Ma, S. Gou, Z. Zhu, J. Sun, M. A. Shahbazi, T. Si, C. Xu, J. Ru, X. Shi, R. L. Reis, S. C. Kundu, B. Ke, G. Nie, B. Xiao, *Adv. Mater.* **2024**, *36*, 2309516.
- [25] R. Xu, L. Huang, J. Liu, Y. Zhang, Y. Xu, R. Li, S. Su, X. Xu, *Small* **2023**, *20*, 2305923.
- [26] L. Galluzzi, A. Buqué, O. Kepp, L. Zitvogel, G. Kroemer, *Nat. Rev. Immunol.* **2016**, *17*, 97.
- [27] Y. Guo, X. Zhang, S. Z. Wang, H. H. Feng, S. Y. Wu, F. G. Wu, *Research* **2023**, *6*, 0052.
- [28] S. Wu, K. Zhang, Y. Liang, Y. Wei, J. An, Y. Wang, J. Yang, H. Zhang, Z. Zhang, J. Liu, J. Shi, *Adv. Sci.* **2021**, *9*, 2103534.
- [29] Y. Wang, F. Gao, L. Zhao, Y. Wu, C. Li, H. Li, Y. Jiang, *Coordin. Chem. Rev.* **2024**, *500*, 215535.
- [30] W. H. Chen, G. F. Luo, Q. Lei, S. Hong, W. X. Qiu, L. H. Liu, S. X. Cheng, X. Z. Zhang, *ACS Nano* **2017**, *11*, 1419.
- [31] S. Liu, Y. Sun, M. Jiang, Y. Li, Y. Tian, W. Xue, N. Ding, Y. Sun, C. Cheng, J. Li, X. Miao, X. Liu, L. Zheng, K. Huang, *Hepatology* **2017**, *66*, 631.
- [32] Q. Li, C. Chen, J. Kong, L. Li, J. Li, Y. Huang, *Acta Pharm. Sin. B* **2022**, *12*, 2533.
- [33] L. Cassetta, J. W. Pollard, *Nat. Rev. Cancer* **2023**, *23*, 238.
- [34] S. Ganapathy-Kanniappan, J. F. H. Geschwind, *Mol. Cancer* **2013**, *12*, 152.
- [35] A. Mantovani, F. Marchesi, A. Malesci, L. Laghi, P. Allavena, *Nat. Rev. Clin. Oncol.* **2017**, *14*, 399.
- [36] Y. W. Choo, M. Kang, H. Y. Kim, J. Han, S. Kang, J. R. Lee, G. J. Jeong, S. P. Kwon, S. Y. Song, S. Go, M. Jung, J. Hong, B. S. Kim, *ACS Nano* **2018**, *12*, 8977.
- [37] T. J. Hayman, M. Baro, T. MacNeil, C. Phoomak, T. N. Aung, W. Cui, K. Leach, R. Iyer, S. Challa, T. Sandoval-Schaefer, B. A. Burtness, D. L. Rimm, J. N. Contessa, *Nat. Commun.* **2021**, *12*, 2327.
- [38] Y. Jiang, X. Li, F. Qian, B. Sun, X. Wang, Y. Zhang, D. Zhang, M. Geng, Z. Xie, S. Yang, *Research* **2023**, *6*, 0102.
- [39] G. N. Barber, *Nat. Rev. Immunol.* **2015**, *15*, 760.
- [40] L. Corrales, S. M. McWhirter, T. W. Dubensky, T. F. Gajewski, *J. Clin. Invest.* **2016**, *126*, 2404.
- [41] L. Corrales, T. F. Gajewski, *Clin. Cancer Res.* **2015**, *21*, 4774.
- [42] J. Wu, Z. J. Chen, *Annu. Rev. Immunol.* **2014**, *32*, 461.
- [43] K. M. Garland, T. L. Sheehy, J. T. Wilson, *Chem. Rev.* **2022**, *122*, 5977.
- [44] Z. H. Wang, M. Chu, N. Yin, W. T. Huang, W. Liu, Z. Z. Zhang, J. J. Liu, *J. Shi, Sci. Adv.* **2022**, *8*, eabn3917.
- [45] M. May, *Nat. Med.* **2022**, *28*, 1100.
- [46] W. Yang, Y. Ma, H. Xu, Z. Zhu, J. Wu, C. Xu, W. Sun, E. Zhao, M. Wang, R. L. Reis, S. C. Kundu, X. Shi, B. Xiao, *Research* **2023**, *6*, 0188.
- [47] D. Napierska, R. Quarck, L. C. J. Thomassen, D. Lison, J. A. Martens, M. Delcroix, B. Nemery, P. H. Hoet, *Small* **2012**, *9*, 430.
- [48] Z. Pei, H. Lei, L. Cheng, *Chem. Soc. Rev.* **2023**, *52*, 2031.
- [49] A. Ribas, J. D. Wolchok, *Science* **2018**, *359*, 1350.
- [50] Y. J. Liu, *Cell* **2001**, *106*, 259.
- [51] Y. Togashi, K. Shitara, H. Nishikawa, *Nat. Rev. Clin. Oncol.* **2019**, *16*, 356.
- [52] Q. Fan, Z. Li, J. Yin, M. Xie, M. Cui, C. Fan, L. Wang, J. Chao, *Biomaterials* **2023**, *301*, 122283.
- [53] G. M. Jiang, Y. Tan, H. Wang, L. Peng, H. T. Chen, X. J. Meng, L. L. Li, Y. Liu, W. F. Li, H. Shan, *Mol. Cancer* **2019**, *18*, 17.
- [54] H. Kayama, R. Okumura, K. Takeda, *Annu. Rev. Immunol.* **2020**, *38*, 23.
- [55] S. H. Wong, J. J. N. R. G. Yu, *Hepatology* **2019**, *16*, 690.
- [56] B. J. Parker, P. A. Wearsch, A. C. M. Veloo, A. Rodriguez-Palacios, *Front. Immunol.* **2020**, *11*, 906.
- [57] Z. Faghfoori, M. H. Faghfoori, A. Saber, A. Izadi, A. Yari Khosroushahi, *Cancer Cell Int.* **2021**, *21*, 258.
- [58] Z. Zhang, H. Cao, N. Song, L. Zhang, Y. Cao, J. Tai, *Food Chem. Toxicol.* **2020**, *138*, 111237.
- [59] C. Xing, M. Wang, A. A. Ajibade, P. Tan, C. Fu, L. Chen, M. Zhu, Z. Z. Hao, J. Chu, X. Yu, B. Yin, J. Zhu, W. J. Shen, T. Duan, H. Y. Wang, R. F. Wang, *Cell Host Microbe* **2021**, *29*, 959.
- [60] S. B. Rifkin, M. A. Sze, K. Tuck, E. Koeppe, E. M. Stoffel, P. D. Schloss, *J. Gastrointest. Cancer* **2023**, *55*, 207.
- [61] S. Gou, Y. Huang, Y. Wan, Y. Ma, X. Zhou, X. Tong, J. Huang, Y. Kang, G. Pan, F. Dai, B. Xiao, *Biomaterials* **2019**, *212*, 39.
- [62] H. Jaeschke, J. J. Lemasters, *Gastroenterology* **2003**, *125*, 1246.
- [63] W. Yue, L. Chen, L. Yu, B. Zhou, H. Yin, W. Ren, C. Liu, L. Guo, Y. Zhang, L. Sun, K. Zhang, H. Xu, Y. Chen, *Nat. Commun.* **2019**, *10*, 2025.
- [64] Q. Liu, Z. Sun, L. Chen, *Protein Cell* **2020**, *11*, 549.